HIGH ENERGY GAMMA-RAY ASTRONOMY OBSERVATIONS OF GEMINGA WITH THE VERITAS ARRAY

by

Gary Marvin Finnegan

A dissertation submitted to the faculty of
The University of Utah
in partial fulfillment of the requirements for the degree of

Doctor of Philosophy

in

Physics

Department of Physics and Astronomy

The University of Utah

December 2012

The University of Utah Graduate School

STATEMENT OF DISSERTATION APPROVAL

This dissertation of
Gary Marvin Finnegan

has been approved by the following supervisory committee members:

David B. Kieda	, Chair	August 22, 2012
		Date Approved
Peter W. Alfeld	, Member	September 13, 2012
		Date Approved
Carleton Detar	, Member	September 12, 2012
		Date Approved
Stephane Louis Le Bohec	, Member	August 22, 2012
		Date Approved
Robert Wayne Springer	, Member	
		Date Approved

and by David B. Kieda, Chair of

the Department of
Physics and Astronomy

and by Charles A. Wright of the Graduate School.

ABSTRACT

The closest known supernova remnant and pulsar is Geminga. The Geminga pulsar is the first pulsar to have ever been detected initially by gamma rays and the first pulsar in a class of radio-quiet pulsars. In 2007, the Milagro collaboration detected a large angularly extended ($\sim 2.6^{\circ}$) emission of high energy gamma rays ($\sim 20\ TeV$) that was positionally coincident with Geminga.

The Very Energetic Radiation Imaging Telescope Array System (VERITAS) is a ground-based observatory with four imaging Cherenkov telescopes with an energy range between 100 GeV to more than 30 TeV. The imaging Cherenkov telescopes detect the Cherenkov light from charged particles in electromagnetic air showers initiated by high energy particles such as gamma rays and cosmic rays. Most gamma-ray sources detected by VERITAS are point like sources, which have an angular extension smaller than the angular resolution of the telescopes ($\sim 0.1^{\circ}$). For a point source, the background noise can be measured in the same field of view (FOV) as the source. For an angularly extended object, such as Geminga, an external FOV from the source region must be used to estimate the background noise, to avoid contamination from the extended source region.

In this dissertation, I describe a new analysis procedure that is designed to increase the observation sensitivity of angularly extended objects like Geminga. I apply this procedure to a known extended gamma-ray source, Boomerang, as well as Geminga. The results indicate the detection of very high energy emission from the Geminga region at the level of 4% of the Crab nebula with a weighted average spectral index of -2.8 ± 0.2. A possible extension less than one degree wide is shown. This detection, however, awaits a confirmation by the VERITAS collaboration.

The luminosity of the Geminga extended source, the Vela Nebula, and the Crab nebula was calculated for energies greater than 1 TeV. The data suggest that older pulsars, such as Geminga and Vela, convert the spin-down power of the pulsar more efficiently to TeV energies than a younger pulsar such as the Crab pulsar.

To my wife Amber, for enduring with me...

CONTENTS

LIST OF TABLES

LIST OF FIGURES

ACKNOWLEDGMENTS

So many people have helped me and continue to show me the way, and for that I am very grateful. I must first give thanks to my long time mentor, Dave Kieda. Nine years ago, I wandered into your office looking for a job as an undergraduate research assistant, and found a relationship that lasted through my entire University education. Thanks Dave!

To Stephane Le Bohec, thanks for listening to all my ideas, whether they were crazy or sane. I still think my Star Base logo design is the best.

A huge thanks to Peter Alfeld, Carleton Detar, and R. Wayne Springer who patiently endured the many edits of this manuscript.

Thanks is not enough for all of my friends that helped me study and pass the required graduate courses. I would like to thank Sagar Godambe, Michelle Hui, Paul Nunez, and Stephane Vincent for an era of friendship while working for the Utah VERITAS group.

Thanks to all of the staff members at the Physics and Astronomy department who always kept me going in the right direction.

CHAPTER 1

INTRODUCTION TO HIGH ENERGY GAMMA-RAY ASTRONOMY

1.1 Introduction

Knowledge of the universe outside of our solar system has come from the observation of photons from astrophysical phenomena. The range of photon energies in the electromagnetic spectrum (sometimes given in units of frequency, or wavelength) spans over 38 orders of magnitude. It is only possible to collect photons on the surface of the Earth in the visible and radio wavelength ranges. Photons in the microwave, infrared, and any with shorter wavelengths than visible light are highly attenuated by the Earth's atmosphere. A visual representation of the electromagnetic spectrum and the bands (sometimes called windows) of photons that can penetrate the Earth's atmosphere is given in Figure 1.1.

Photons with energies higher than ultraviolet energies do not directly penetrate the Earth's atmosphere. Photons with energies greater than ~ 83 MeV (1 MeV $= 10^6$ eV), and even high energy cosmic rays, will create an electromagnetic shower of charged particles as they collide with particles in the atmosphere. The Nobel Laureate P.M.S. Blackett first reported to the Royal Society (Blackett 1948) of the possibility that cosmic rays are contributing to light of the night sky by means of Cherenkov radiation.

Galbraith & Jelley (1953) followed up on this idea by Blackett. Galbraith and Jelley mounted a photomultiplier tube (PMT) and a parabolic mirror inside a metal garbage can, a crude telescope, with the signal output of the PMT sent through an amplifier and then into an oscilloscope. They measured the noise level of the night sky by monitoring the electrical current through the PMT. They recorded on the oscilloscope a pulse every few minutes with a pulse height several times greater than signal created by the night sky. They verified that the pulses were not artificially created. They did this by placing the lid on the telescope and by using a small lamp inside to reproduce the electrical current in the PMT that was created from the night sky background light. No pulses were seen in the

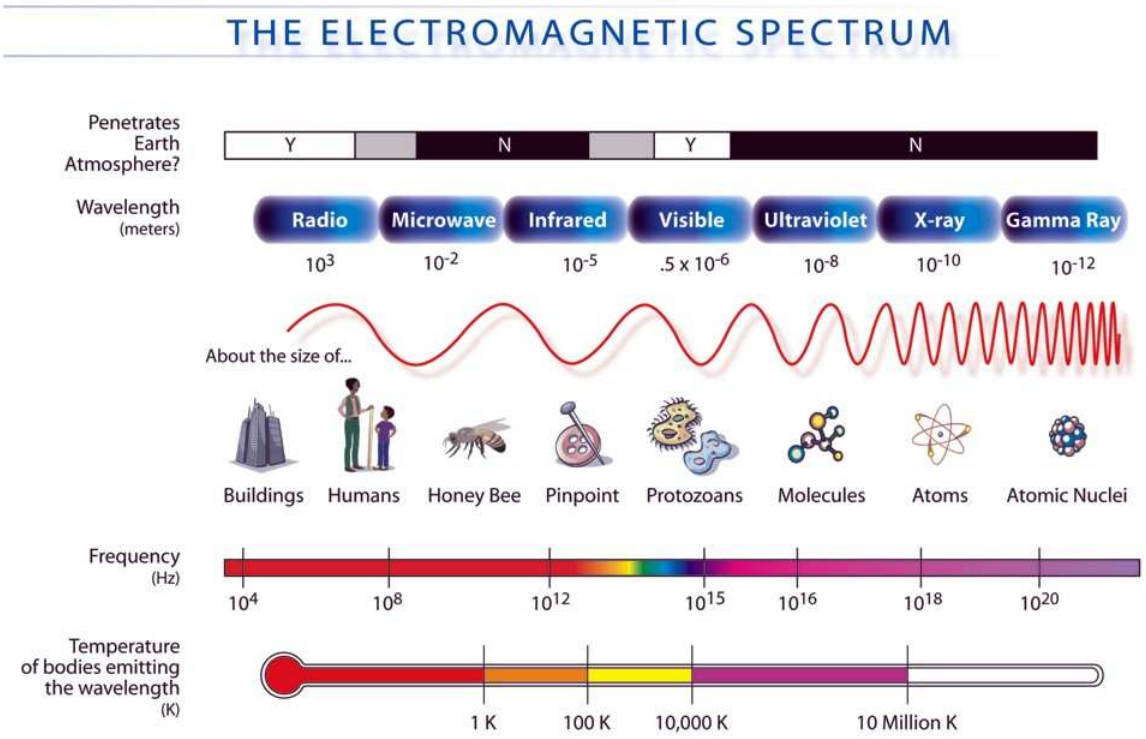

Figure 1.1. The electromagnetic spectrum. The top bar shows which photon windows are open for ground level observations. Other diagrams illustrate the size, frequency, and temperature of the corresponding photon. Credit: NASA (via https://mynasadata.larc.nasa.gov)

50-minute test with the lid on the telescope. They had observed the Cherenkov radiation given off by highly energetic charged particles that were energized by the collision of the incoming gamma rays or cosmic rays with the nuclei of the atoms in the atmosphere. This was the start of the atmospheric Cherenkov techniques, which will be discussed later in the chapter.

1.2 Very High Energy Gamma-Ray Astronomy

Traditionally, photons with energies higher than 10^6eV ($\sim 1.6 \times 10^{-13}$ $joules$) are called gamma rays. Gamma rays in the energy band from 10^6eV to 10^9eV are designated as high energy (HE) gamma rays; photons with energies greater than 10^9eV are called very high energy (VHE) gamma rays. HE and VHE gamma ray emission mechanisms may have links to cosmic ray acceleration. Three important astrophysical gamma-ray production mechanisms are synchrotron radiation (Alfvén & Herlofson 1950), inverse Compton scattering (Blumenthal & Gould 1970), and π^0 decay (Cavallo & Gould 1971). Synchrotron radiation and inverse Compton scattering provide evidence of electron acceleration whereas π^0 decay provides evidence of the acceleration of VHE cosmic rays.

1.2.1 Very High Energy Galactic Astrophysical Objects

Cosmic-ray spectra cover many decades of energy. According to Garcia-Munoz et al. (1977), the mean lifetime of a galactic cosmic ray, by measuring the half-life of Beryllium-10 nuclei, is on the order of 10^7 years. In order to maintain the observed flux of galactic cosmic rays, a cosmic ray replenishment rate of approximately $10^{41} ergs\ s^{-1}$ (Weekes 2003) ($1erg = 10^{-7} Joules$) is needed. One of the fundamental ideas of cosmic ray research is to discover the sources within the galaxy that can provide the necessary cosmic ray replenishment rate to maintain the observed flux.

Early TeV gamma-ray astronomy experiments were fueled by the desire to discover the origin of galactic cosmic rays. Astrophysical objects such as supernova remnants, pulsars, pulsar wind nebulae, and high mass X-ray binary objects are excellent candidates for acceleration of charged particles. Active galactic nuclei (AGN) and starburst galaxies have also been thought of as sites of ultra-high energy cosmic ray acceleration, although they are extragalactic in origin. Astronomers expected that if particles were being accelerated in particular astrophysical objects, a gamma-ray signature from the collisions could be possible to detect. Detection of high energy gamma rays from these object would therefore

help astronomers to locate the acceleration sites of cosmic rays.

1.2.1.1 Supernova Remnants

Supernova Remnants (SNRs) are the remains of massive star explosions. SNRs have been categorized into two general types: type I and type II; each has its own subtypes. Type I SNRs are absent of hydrogen lines in the optical spectrum whereas type II have hydrogen lines. One can categorize SNRs by the way the explosion was ignited into two categories: type Ia, and core collapse SNRs. Type Ia occurs in a binary system with a white dwarf star and a massive companion star. Accretion of mass from the companion star to the white dwarf causes the white dwarf to pass the Chadrasekhar limit of approximately $1.4M_{\odot}$ ($M_{\odot}$ = solar mass). At this point, the carbon center of the white dwarf ignites and causes an explosion that completely disrupts the star. This explosion also causes the mass of the star to accelerate radially outward and form a massive shock front. An example of a type Ia supernova remnant is Tycho's SNR. The flux of VHE gamma rays are relatively low compared to other high energy astrophysical objects. Figure 1.2 shows the Tycho SNR with a composite image of X-ray observations by the Chandra X-ray space-based observatory.

Core collapse SNRs (type II and other type I supernovae) require that the progenitor star be more massive than $8_{M\odot}$. In these massive stars, hydrogen burning (nuclear fusion of hydrogen atoms into helium) leads to a helium core, which eventually begins burning. The helium burning creates heavier particles such as oxygen, neon, sodium, and magnesium. Further gravitational collapses cause the carbon core to ignite, which eventually leads to silicon burning (fusion with helium to create heavier particles). During silicon burning, the temperature of the star will begin to decrease due to photodisintegration, an endothermic process that creates subatomic particles such as protons and neutrons from the disintegration of nuclei. The free protons then combine with the free electrons to produce neutrons, effectively reducing the internal pressure due to loss of electron degeneracy pressure. The star begins to collapse when the thermal pressure and electron degeneracy pressure are less than the pressure gradient due to the gravitational force of the star. Because the density of the inner core is much greater than that of the outer core, the inner core collapses faster than the outer core. When the density exceeds three times the density of the atomic nucleus, neutron degeneracy pressure creates a pressure wave outward from the inner core. The pressure wave contacts the collapsing outer core, reversing its direction and creating a shock front. What is left is a neutron star and a shock front, or shell. Both types of

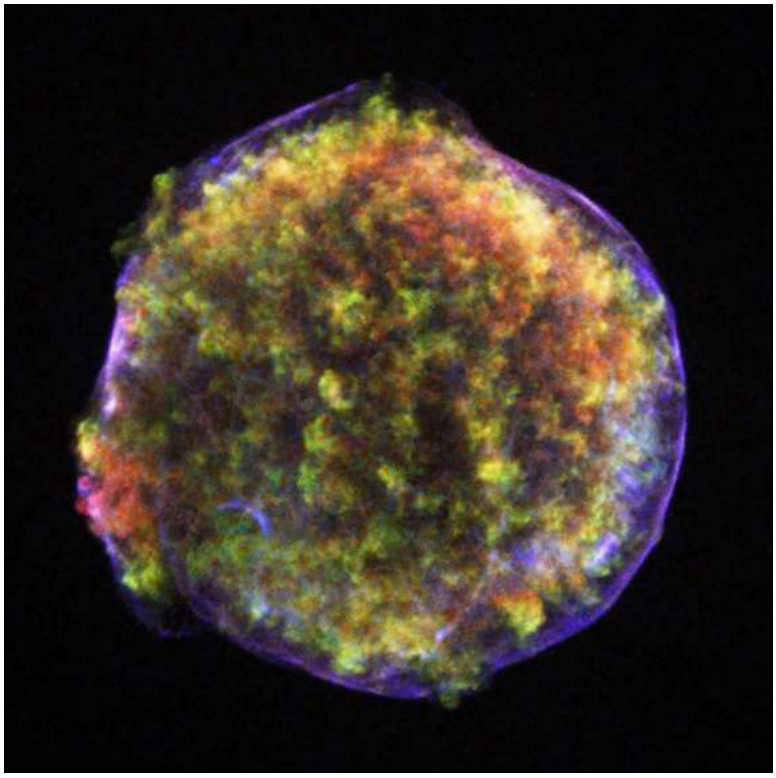

Figure 1.2. Composite X-ray image of the Tycho SNR taken by the Chandra X-ray observatory. The blue filaments show the extrememly high energy electrons. The red and green remnant material is multimillion degree debris from the SNR. Credit: NASA/CXC/Rutgers/J.Warren & J.Hughes et al.

SNRs release about the same amount of maximum energy of approximately $10^{41} ergs\ s^{-1}$. It is hypothesized that SNRs are replenishing the lower energy cosmic rays in the galaxy (Weekes 2003).

1.2.1.2 Pulsars

It was first suggested by Gold (1968) that pulsars are rapidly rotating magnetized neutron stars, with a co-rotating magnetic field (see Figure 1.3). When the beam of electromagnetic radiation passes an observer due to the neutron star's rotation, a pulse is seen across the electromagnetic spectrum from radio to gamma rays.

Two observables from pulsars are their periods and period derivatives. Pulsar periods, in the absence of accretion, gradually slow down due to electromagnetic radiation. Assuming the magnetic field of a pulsar can be approximated by a magnetic dipole, one can estimate the radiative energy loss by measuring the period and the period derivative. The rate of energy loss of rotational kinetic energy is

$$\dot{E}_{rot} = \frac{dE_{rot}}{dt} = \frac{d}{dt}\left(\frac{1}{2} I\Omega^2\right) = I\Omega\dot{\Omega}, \tag{1.1}$$

where I is the moment of inertia, and Ω is the angular frequency. One can convert Ω into the period by $\Omega = 2\pi/P$. This gives rise to the spin-down equation:

$$\dot{E}_{rot} = \frac{dE_{rot}}{dt} = -\frac{4\pi^2 I\dot{P}}{P^3}. \tag{1.2}$$

Higher $\dot{P}$ pulsars radiate more energy and therefore make better candidates for high energy emission. If one assumes that the energy loss in a pulsar is due to the dipole radiation (Lorimer & Kramer 2005),

$$\dot{E} = \frac{2}{3c^3}|\vec{m}|^2\Omega^4 \sin^2\alpha, \tag{1.3}$$

where α is the inclination angle between the rotational pole and the magnetic pole and $|\vec{m}|$ is the magnetic dipole moment.

A characteristic age may be found by taking the power radiated by a rotating magnetic dipole and comparing it to the rate loss of rotational kinetic energy

$$\frac{2}{3c^3}|\vec{m}|^2\Omega^4 \sin^2\alpha = \frac{d}{dt}\left(\frac{1}{2} I\Omega^2\right) = I\Omega\dot{\Omega}. \tag{1.4}$$

The above equation can be simplified by defining

$$K = \frac{2}{2Ic^3}|\vec{m}|^2 \sin^2\alpha, \tag{1.5}$$

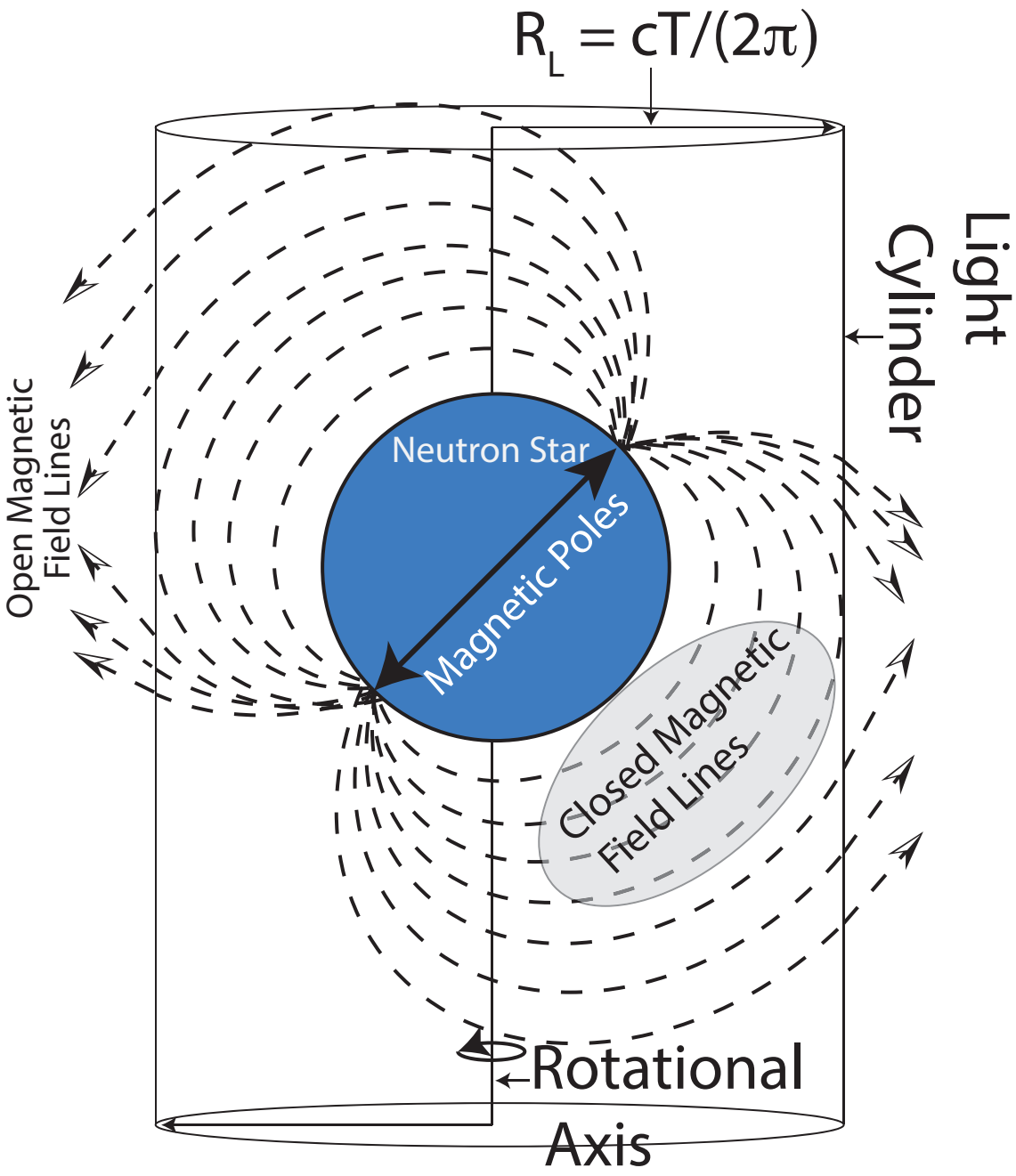

Figure 1.3. A diagram of a pulsar showing the open and closed magnetic field lines from the light cylinder.

where K is a constant. This gives

$$\dot{\Omega} = K\Omega^n, \tag{1.6}$$

where n, the braking index, equals 3. A perfect rotating magnetic dipole has a braking index of 3. For a more general case, Equation (1.6) can be rewritten in terms of the rotational frequency $\nu = 1/P$,

$$\dot{\nu} = K\nu^n, \tag{1.7}$$

or in terms of the period,

$$\dot{P} = KP^{2-n}. \tag{1.8}$$

The above differential equation can be solved for t (time) to determine the characteristic age of the pulsar. The resulting solution is

$$t = \frac{P}{(n-1)\dot{P}}\left[1 - \left(\frac{P_0}{P}\right)^{n-1}\right]. \tag{1.9}$$

If one assumes that the period at birth of the pulsar (P_0) was much shorter than the current period, a pulsar braking index $n = 3$, then Equation (1.9) reduces to

$$t = \frac{P}{2\dot{P}}. \tag{1.10}$$

The Crab pulsar's period of 33 ms and period derivative of $4.2 \times 10^{-13} s/s$, (Abdo et al. 2010a) gives a characteristic age of approximately 1245 years. The actual age of the Crab pulsar is approximately 1000 years. The characteristic age of a pulsar gives a good order of magnitude estimation of the age of the supernova .

Gold suggested that the observed electromagnetic pulses were due to charged particles following the open magnetic field lines at the light cylinder. The light cylinder is a non-physical cylinder that has a radius, $R_L = \frac{1}{2\pi}cT$ (Figure 1.3). Any particle following the magnetic field outside of the radius R_L would be required to travel faster than light to intersect with the opposite pole of the pulsar. Therefore, any magnetic field lines are open at a distance of R_L from the pulsar.

Three major models of a pulsar's pulsed emission have been developed based on Gold's simplified model. The polar cap model was developed by Goldreich & Julian (1969) and in more detail by Sturrock (1971). Particles are accelerated at the polar region of the polar cap model near the surface of the neutron star. Many variations of the polar cap model exist. Depending on the variation, the high energy electromagnetic radiation can come from electron positron pair annihilation or by particle acceleration due to the force of the electric

field pulling the charged particles from the surface of the star. The polar cap model predicts a hollow polar cap emission cone that gives rise to the observed double peak pulsar light curve.

The second major model is the outer gap model. Cheng et al. (1986) suggested that a vacuum is created between charged depleted areas and opened magnetic field lines with a strong electric field. The force due to the electric field on the charged particles accelerates the particles to relativistic velocities. The gamma rays can then be radiated due to inverse Compton scattering, curvature radiation, or synchrotron radiation. A fan beam (a beam originating at the light cylinder due to open magnetic field lines) is predicted with the outer gap model.

The third model is the slot gap model (Arons 1981). The slot gap model is a composite of the polar cap and the outer gap model. The location of the gap begins at the poles and extends to the light cone (Figure 1.4). The acceleration of particles is near the last closed magnetic field line.

The detailed mechanisms at play in pulsars are still quite a mystery. The models can be distinguished by the spectral differences of VHE gamma-ray emission. The most energetic particles are believed to be accelerated high in the magnetosphere. Most pulsar energy spectra can be fitted to a power-law fit with a cutoff in energy. For the polar cap model, a super-exponential cutoff in the higher energies is believed to exist due to the lower altitude acceleration of the charged particles. The slot gap model also has a super-exponential cutoff due to emission height from the neutron star. The outer gap model has an exponential cutoff which extends to higher energy than the previous two models. None of these models perfectly predict the observed flux of all known pulsars.

Recently, the VERITAS collaboration reported a detection of the Crab pulsar above 100 GeV (VERITAS Collaboration et al. 2011). They found a cutoff in energy (Figure 1.5) of the Crab pulsar spectrum to be more consistent with a broken power law; this does not correspond to any of the known models. It was suggested by the VERITAS Collaboration (2011) that the observed flux might be explained by inverse Compton scattering. The presence of HE pulsed emission seems to rule out the existence of pulsed gamma-ray emission by curvature radiation.

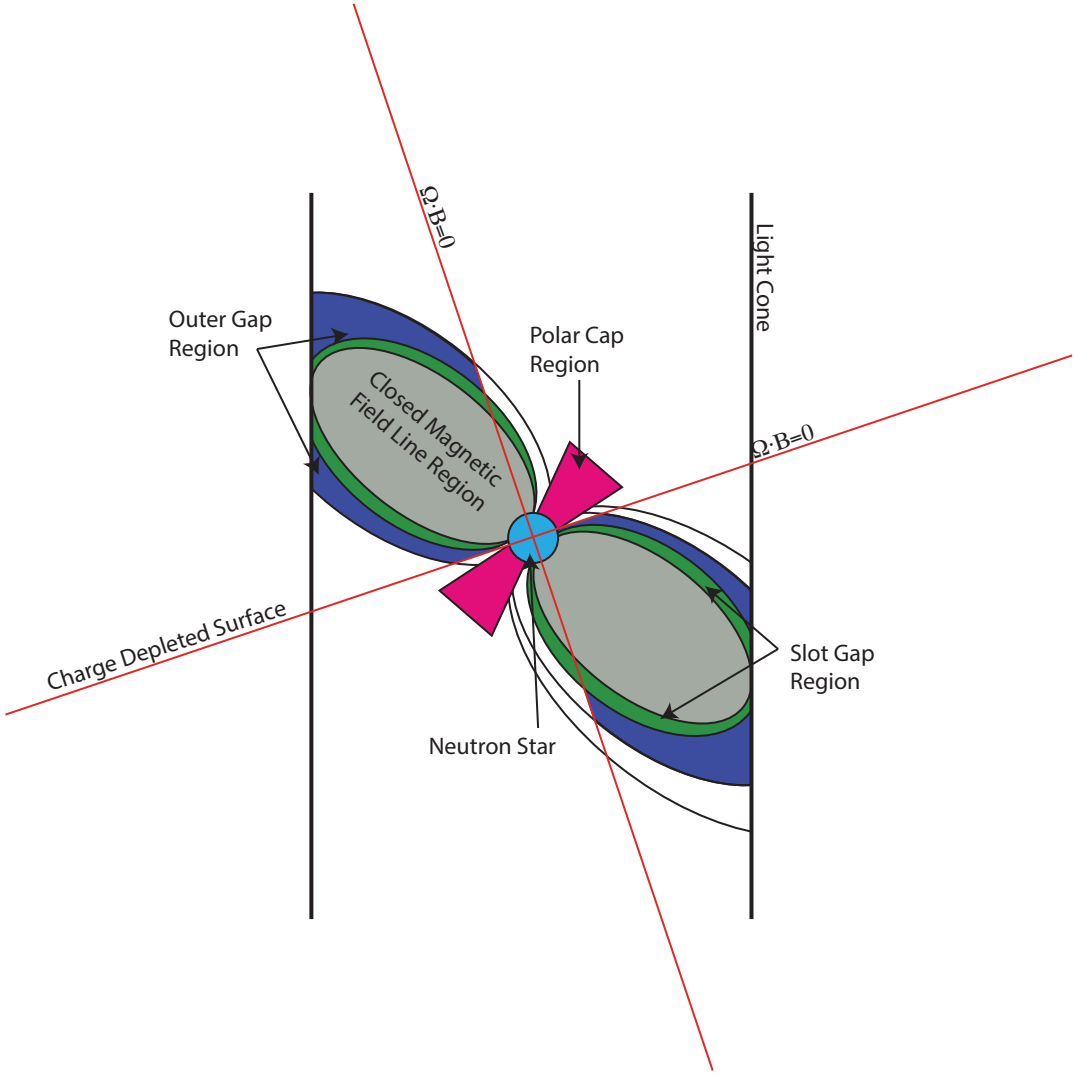

Figure 1.4. The three major models, polar cap (pink), outer gap (blue) and slot gap (green) models accelerate the particles in different physical regions of a pulsar.

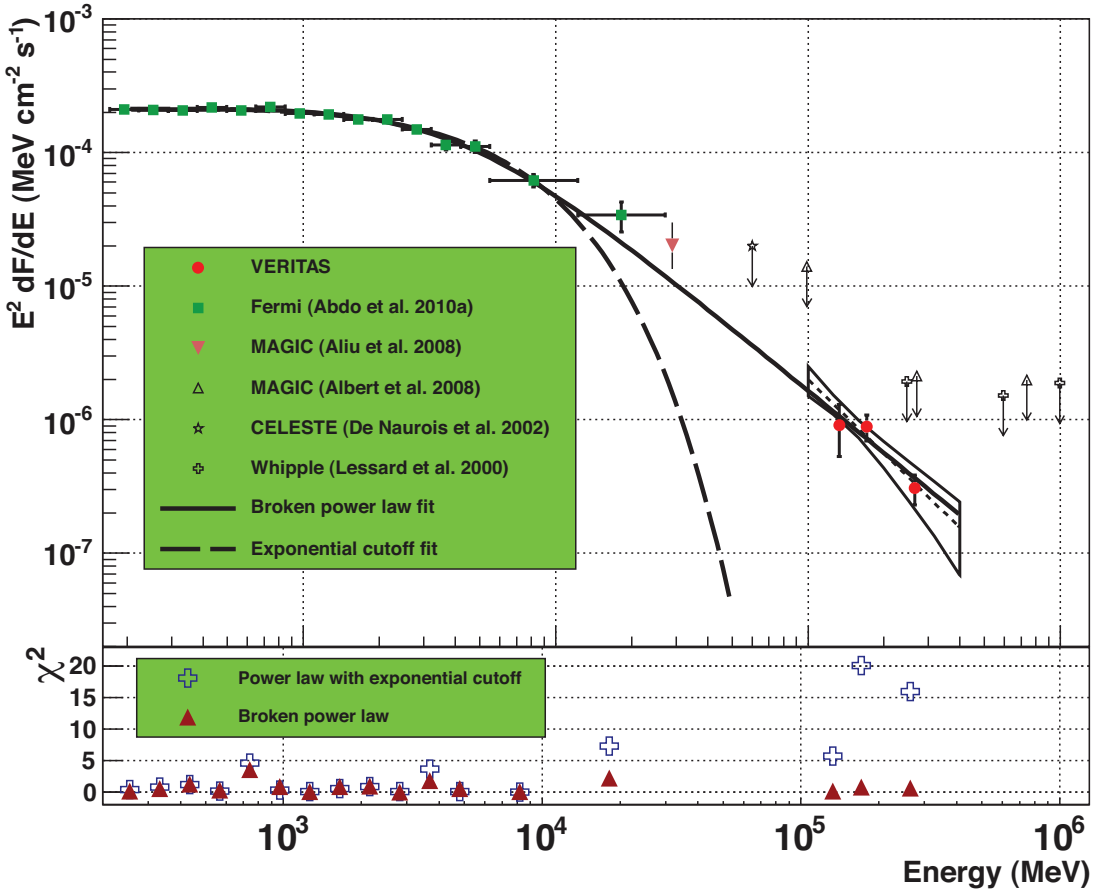

Figure 1.5. Spectral energy distribution of the Crab pulsar over four decades of energy (MeV), showing the power-law fits with a broken power-law and an exponential cutoff. (VERITAS Collaboration et al. 2011)

1.2.1.3 Pulsar Wind Nebulae

Pulsar wind nebulae (PWNe) (Gaensler & Slane 2006) consist of a pulsar and a surrounding interstellar medium, usually consisting of the supernova remnant shell or a molecular cloud. The Crab nebula (referring to the entire nebula, which includes the pulsar) is an example of a PWN. The accelerated particles from the pulsar's magnetosphere interact with the rich interstellar medium. PWNe receive most of their energy from the pulsars spin-down energy. There are two important high energy radiative processes in PWNe. The first is synchrotron radiation and the second is inverse Compton scattering. Synchrotron radiation is radiation emitted by relativistic electrons in a magnetic field. Synchrotron radiation can produce gamma rays with energies up to the GeV range. For the GeV energy range and higher, inverse Compton scattering dominates. Inverse Compton scattering occurs when low energy photons are scattered off relativistic electrons or positrons. In this case, the photons gains energy and the charged particles lose some of their energy.

IC 443 is an example of a PWN that includes interactions with a remnant shell and a molecular cloud. Analysis of the VERITAS IC 443 data shows a soft spectral index of $-2.99 \pm 0.38_{stat} \pm 0.30_{sys}$ and a flux of $(4.63 \pm 0.90_{stat} \pm 0.93_{sys}) \times 10^{-12} cm^{-2} s^{-1}$ above 300 GeV (Acciari et al. 2009) (Figure 1.6). Location of the VHE emission is seen in the region with the molecular cloud (Figure 1.7).

1.2.1.4 High Mass X-ray Binary Objects

High Mass X-ray Binaries (HMXBs) are X-ray sources which contain a massive star and a compact object (such as a neutron star or black hole) in mutual orbit. In some models of HMXBs, an accretion disk is formed around the compact object due to the Roche overflow of the massive companion star. As the mass is pulled towards the center of the compact object, the accretion disk begins to heat from compression temperatures greater than 10^6 K, resulting in X-ray emission. HMXBs can also emit VHE gamma rays. Many models use synchrotron emission to inverse Compton scattering to explain the observed VHE gamma-ray flux. One of the difficulties in explaining the origin of VHE gamma rays from HXMBs is that only four HMXBs have been detected by VHE experiments: LSI +61 303, LS 5039, PSR B1259-63, and HESS J0632+057.

HESS J0632+057 was first detected in VHE gamma rays by the HESS collaboration. It is a weak X-ray source, but despite the weak X-ray emission, the evidence is suggesting that it is a HMXB (Aharonian et al. 2007). Periodic behavior is seen in the emission of VHE

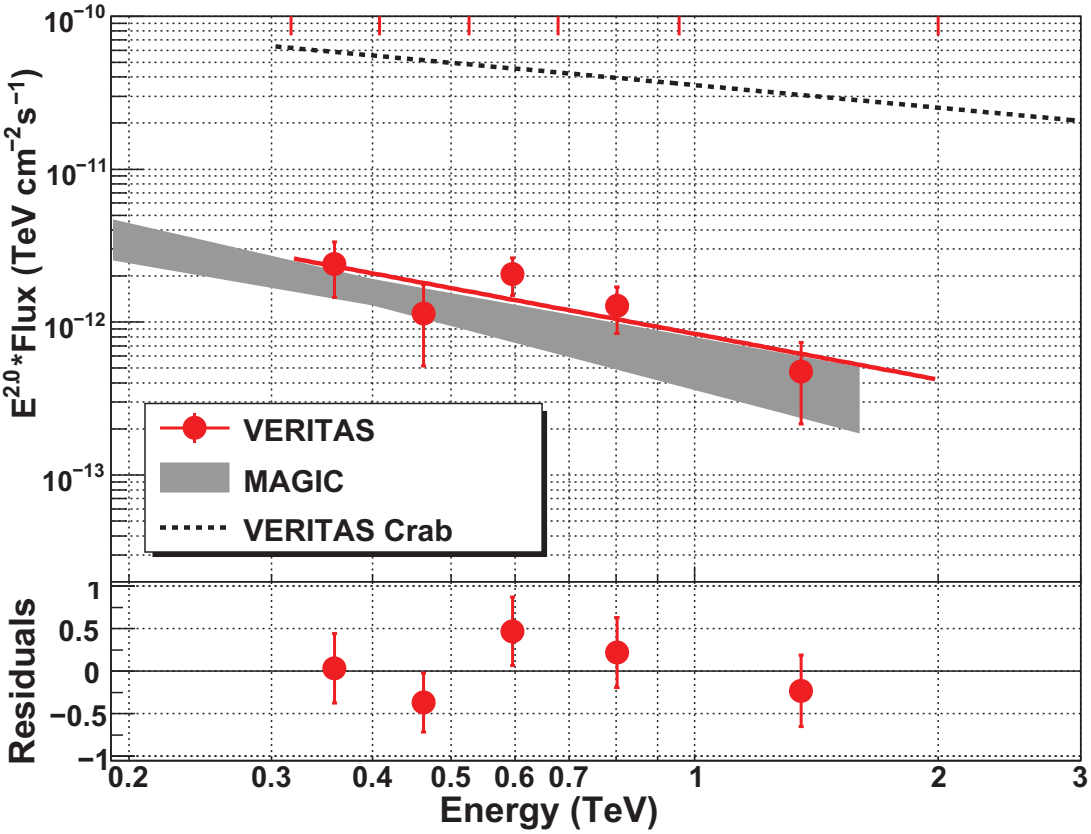

Figure 1.6. Spectrum of IC 443, scaled by E^2. Red points are the VERITAS spectral data points (top) with a fitted power-law, and residuals (bottom). The grey region is the measured flux above 90 GeV by the MAGIC collaboration (Albert et al. 2007), and the dashed line is the Crab nebula spectrum (The VERITAS Collaboration 2012, in preparation).

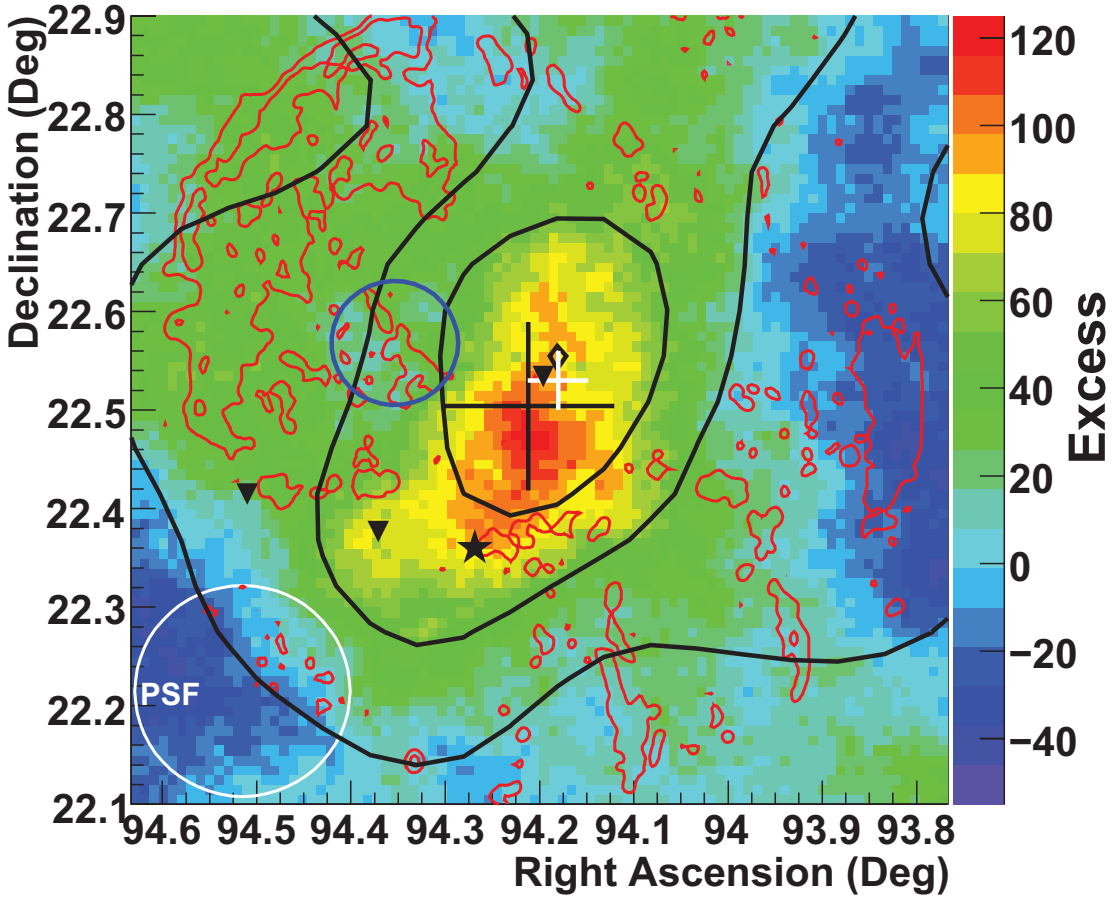

Figure 1.7. IC 443 excess map ($E > 300GeV$) (Acciari et al. 2009). The black circle indicates the one-sigma angular extension. The black cross-hair indicates the centroid position and its uncertainty (statistical and systematic added in quadrature), and the white cross-hair indicates the position and uncertainty of MAGIC J0616+225 (Albert et al. 2007). Red countours: optical intensity (McLean et al. 2000). The white circle represents the point spread function (PSF) of VERITAS. Thick black contours: OC survey (Huang & Thaddeus 1986); black star: PWN CXOU J061705.3+222127 (Olbert et al. 2001); open blue circle: 95% confidence radius of 0FGL J0617.4+2234 (Abdo et al. 2009c); and filled black triangles: locations of OH maser emission (Claussen et al. 1997).

gamma rays due to the binary nature of the HMXB. The HESS collaboration has detected LS 5039 in VHE gamma rays with a 3.9-day period (de Naurois 2007). They also detected PSRJ B1259-63 with a high energy emission around periastron. A periodicity of 321 ± 0.5 days was recently found by Bongiorno et al. (2011) from HESS J0632+057 with the Swift X-ray Telescope data. Recent VHE observations of LSI +61 303 by VERITAS show orbit to orbit (26.5-day period) variations in the VHE emission (Maier 2011). TeV gamma-ray detections near apastron (Acciari et al. 2008) and near periastron (Maier 2011) have been observed.

1.2.2 Very High Energy Extra-Galactic Astrophysical Objects

The center of our galaxy contains a supermassive ($\sim 10^8 M_\odot$) black hole (Schödel et al. 2002), Sgr A*. Observation of other active galaxy nuclei can provide an unobstructed view of the high energy process associated with supermassive black holes similar to our own. With the low rate SNRs in our own galaxy, viewing starburst galaxies where SNRs are frequent will add to the knowledge of cosmic ray acceleration through supernovae.

1.2.2.1 Active Galactic Nuclei

Active galactic nuclei (AGN) consist of a compact object, thought to be a supermassive black hole centered in an active galaxy, a collimated outflow of relativistic particles forming two jets, each on opposite sides of the compact object, and an optically thick dust torus (Weekes 2003) (see Figure 1.8). AGN are highly luminous from the radio to gamma ray spectrum. Active galaxies have been subcategorized depending on spectral emission and angle of the jets relative to the observer. Active galaxies fall under two major classifications: either radio-quiet or radio-loud. The majority of AGN are radio-quiet. Within the radio-loud AGNs are the blazars. Blazars have a jet that is aligned or slightly misaligned with observers' point of view. Blazars can be extremely strong gamma-ray sources with rapid episodic emission.

1.2.2.2 Starburst Galaxies

Starburst galaxies have a high rate of supernova explosions and massive-star winds. They are galaxies with an abundance of gas that allows a high rate of star formation. They are highly luminous in the infrared spectrum, and have extended areas of X-ray and radio

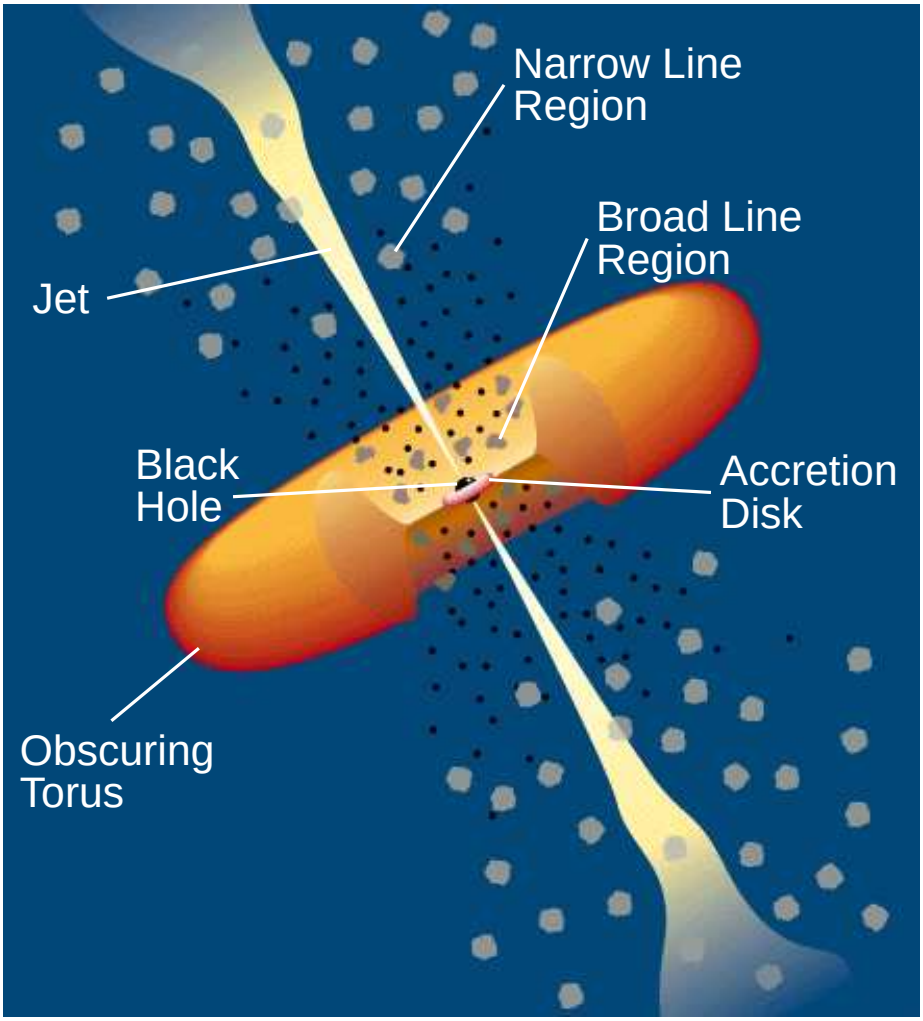

Figure 1.8. A diagram of a theoretical model of a radio-loud AGN. The broad and narrow lines refer to radio emission. The active galaxy would surround this object and is not shown in the diagram. Credit: NASA/GSFC/C.M. Urry & P. Padovani

emission. A famous starburst galaxy is M82, which is nearby the spiral galaxy of M81. For hundreds of millions of years, M82 has been interacting gravitationally with M81(Yun et al. 1994), creating a star forming region (Völk et al. 1996) at its center. M82 and NGC 253 are the two closest starburst galaxies. Because of their high rate of supernova explosions, they are excellent candidate sources for cosmic ray acceleration.

Recently, both M82 (VERITAS Collaboration et al. 2009) and NGC 253 (Acero et al. 2009) have been detected in the gamma-ray energy range. The VERITAS Collaboration (2009) reported gamma rays with an energy greater than 700 GeV. From their data, they estimated that the cosmic-ray density of the starburst galaxy is about 500 times greater than the Galactic density. This possibly links cosmic-ray acceleration to star formation activity, and suggests that supernovae and massive-star winds are the dominant accelerators.

1.2.2.3 Very High Energy Astrophysical Objects: Section Conclusion

All of the aforementioned astrophysical sources are complicated systems of particle acceleration and photon emission. Models describing the acceleration of particles in astrophysical sources are still being developed and tested with the data from recent observations. While many of the these astrophysical objects have strong evidence of particle acceleration, the origin of the highest energy cosmic rays remains controversial.

1.3 Ground-based Gamma-ray Astronomy Techniques

Ground-based techniques are typically divided into two categories: the imaging atmospheric Cherenkov technique, and extensive air shower (EAS) arrays. Telescopes built for the imaging atmospheric Cherenkov technique idea are often called Imaging Atmospheric Cherenkov Telescope arrays or IACT arrays. IACT arrays consist of several independent telescopes separated by $\sim 100m$ each, providing an effective collection area on the order of $10^5 m^2\ sr$. EAS arrays, such as the High Altitude Water Cherenkov (HAWC) experiment, have a physical size on the order of 100 meters, making the effective collection area of $10^5 m^2\ sr$ equivalent.

1.3.1 Imaging Atmospheric Cherenkov Technique

The imaging atmospheric Cherenkov technique relies on two physical ideas, extensive air showers and Cherenkov radiation, which are discussed below. The IACT telescope images the Cherenkov radiation that is produced by extensive air showers initiated by gamma rays and cosmic rays. The atmosphere viewed by the IACT telescope is used as a large calorimeter in which the energy of the shower can be estimated. Parameters of the EAS are compared with parameters that are determined from Monte Carlo simulations to determine if the EAS was initiated by a gamma ray or a cosmic ray and the energy of the primary particle of the EAS.

1.3.1.1 Extensive Air Showers

Heitler (1954) produced the first simplified models of EASs. When a high energy photon enters the atmosphere, it creates an EAS of particles that stream towards the ground (see Figure 1.9). The primary particle, in this case the gamma ray, interacts with the nucleus of an atom in the atmosphere and creates a electron-positron pair, each with approximately half of the energy of the photon. The electron and positron then give rise to to a secondary high energy photon through the Bremsstrahlung radiation process. The energy lost per radiation length due to Bremsstrahlung radiation is given by Longair (2011) of

$$-\frac{dE}{dX} = \frac{E}{X_0}. \tag{1.11}$$

X_0 is defined as the radiation length and has a value of 37.1 $g\ cm^{-2}$ (the units are in dimensions of density times distance, $g\ cm^{-3} \times cm = g\ cm^{-2}$) (Weekes 2003) for an electron traveling through the air. The radiation length of a high energy photon, i.e., the average distanced traveled before pair producing, in air for electron-positron pair production is approximately equal to 40 $g\ cm^{-2}$ (Longair 2011). The atmospheric depth, measured vertically, above sea level is approximately 1030 $g\ cm^{-2}$ (Weekes 2003), which is between 25 and 38 radiation lengths for Bremsstrahlung and pair production. The energy loss due to Bremsstrahlung is given by solving Equation (1.11), and is simply $1/e \sim 0.37$ times the energy of the electron or positron per radiation length. Bremsstrahlung radiation will continue until the energy of the electron reaches ionization energies. The critical energy (E_c) where ionization radiation energy loss starts to dominate is approximately 83 MeV (Bethe & Heitler 1934). When the average shower particles reach E_c, the greatest number of particles is produced (N_{max}) and is said to be at shower max (X_{max}) at a height of h_{max}.

The number of particles (n) before shower max per radiation length is 2^n, and the average energy of the particles at each radiation length is $E_0/2^n$. After the EAS passes shower max, the number of particles decrease. Table 1.1 (Weekes 2003) lists a set of shower parameters for six decades of gamma-ray energies generated by Monte Carlo simulations. The number of particles surviving at sea level ($N_{sea\ level}$) and the number of particles surviving at a mountain observatory height (N_{mnt}) of 2600 meters is given in Table 1.1. The photons surving at sea level and at mountain observatory height ($p_{sea\ level}$ and p_{mnt}) are also given in Table 1.1. Due to the low number of surviving photons and particles at lower altitudes, such as sea level, experiments are best localized at higher altitudes.

When a high energy cosmic ray enters the atmosphere, it will initiate an EAS. The majority of cosmic rays are protons. Proton initiated EASs have similar parameters to a gamma ray initiated EAS. The first interaction produces a set of hadronic particles, mainly pions (π^0, π^+, π^-). A π^0 will decay into two gamma rays. The gamma rays will then pair produce electrons and positrons. The electrons and positrons produced from the shower will initiate an EAS that is similar to that of a gamma ray induced air shower. Figure 1.10 shows a representation of the first few interactions in the proton initiated EAS. A proton EAS in general will have a lower shower maximum altitude than that of gamma rays of the same energy. Figure 1.11 shows a comparison between the EAS of a 320 GeV gamma ray to a 1 TeV proton EAS.

1.3.1.2 Cherenkov Radiation

When a charged particle travels through a neutral dielectric medium with a velocity (v) greater than c/n, where c is the speed of light and n is the index of refraction for the medium, Cherenkov radiation occurs. The Cherenkov radiation is due to the polarization of the surrounding molecules that oscillates on and off, which in turn causes the charged particle to radiate. The Cherenkov radiation is projected in the direction of travel of the charged particle, which traces out a cone like pattern where the opening angle of the cone is given by $\cos\theta = (n/c)/v$ (Figure 1.12).

The Cherenkov radiation spectrum is proportional to a λ^{-2} power law, where λ is the wavelength. The maximum wavelength is approximately 330 nm. As the Cherenkov light propagates through the atmosphere, it will be scattered by means of Mie/Rayleigh scattering. The scattered light intensity ($dI/d\lambda$) is proportional $\lambda^{-4}R^{-2}$ where R is the distance from the initial scattering to the observer, and is nonisotropic.

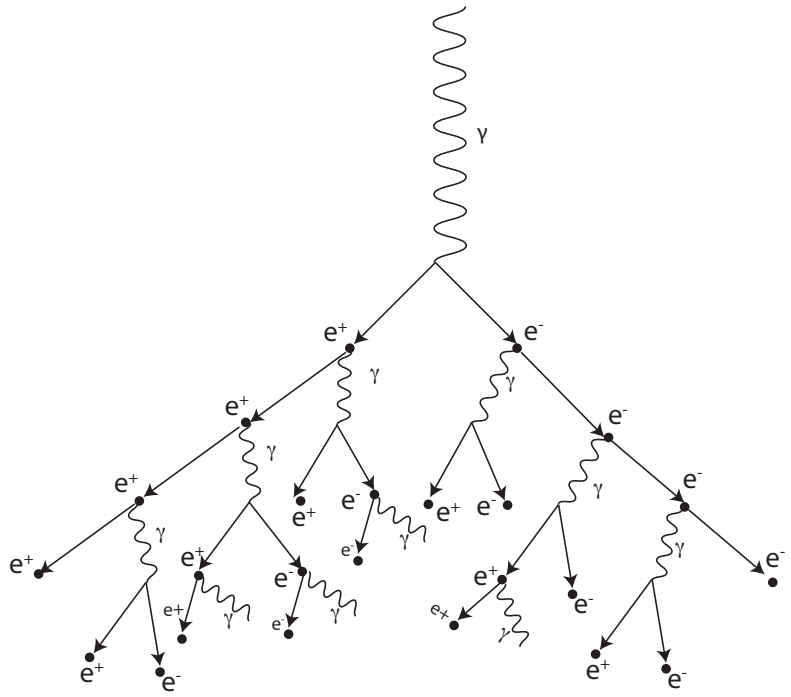

Figure 1.9. Gamma-ray initiated electromagnetic shower produces electron positron pairs, which in turn through Bremsstrahlung radiation produces more gamma rays.

Table 1.1. Gamma-ray initiated extensive air shower parameters as a function of energy derived from Monte Carlo simulations (Weekes 2003)

Energy	X_{max} ($g\ cm^{-2}$)	h_{max} (km)	N_{max}	$N_{sea\ level}$	N_{mnt}	$p_{sea\ level}$ ($\gamma\ m^{-2}$)	p_{mnt} ($\gamma\ m^{-2}$)
1 PeV	602	4.4	8.6×10^5	1.15×10^5	5.7×10^5	1.9×10^5	1.9×10^5
100 TeV	517	5.5	9.3×10^4	4.5×10^3	3.6×10^4	1.6×10^4	1.9×10^4
10 TeV	431	6.8	1.0×10^4	1.3×10^2	1.7×10^3	1.1×10^3	1.7×10^3
1 TeV	346	8.4	1.1×10^3	3.0×10^0	6.0×10^1	7.4×10^1	1.3×10^2
100 GeV	261	10.3	1.3×10^2	4.0×10^{-2}	1.4×10^0	4.6×10^0	7.6×10^0
10 GeV	175	12.8	1.6×10^1	4×10^{-4}	2×10^{-2}	2.7×10^{-1}	3.6×10^{-1}

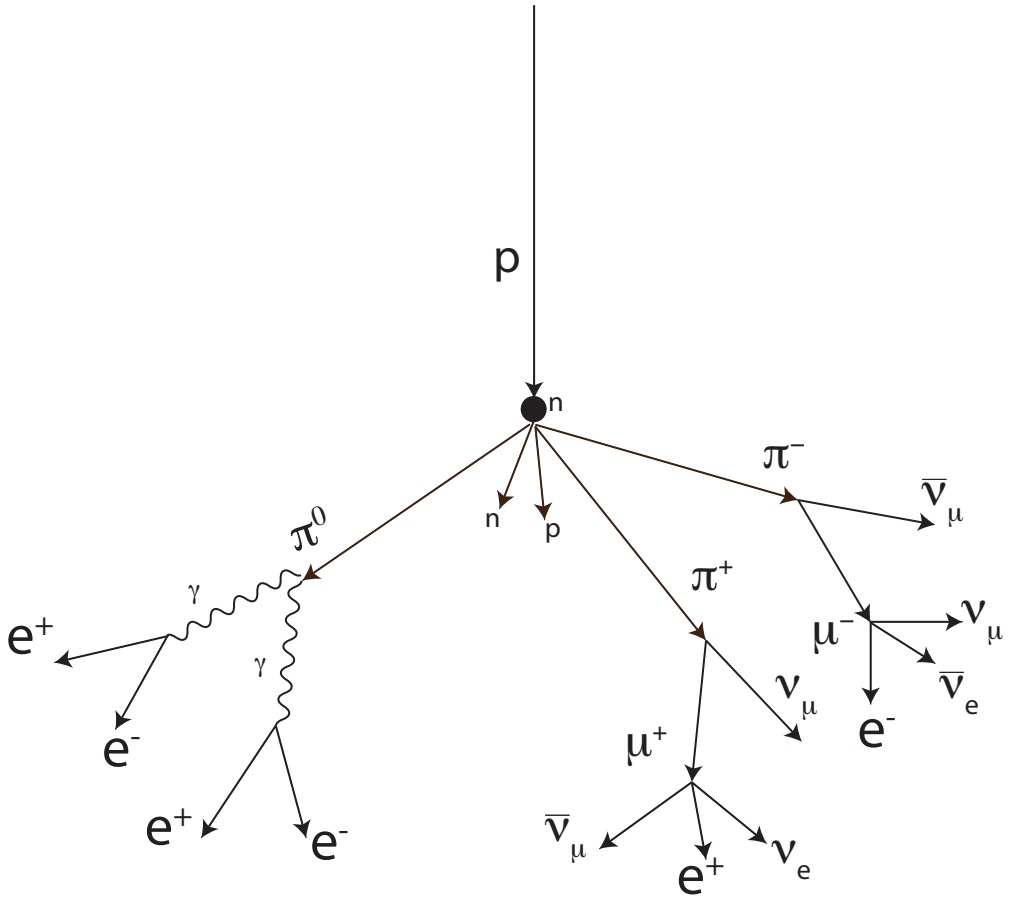

Figure 1.10. A proton initiated electromagnetic air shower produces a hadronic shower of particles of pions, muon, electrons, positrons, and neutrinos. The electrons and positrons will create an EAS that is similar to a gamma-ray induced EAS.

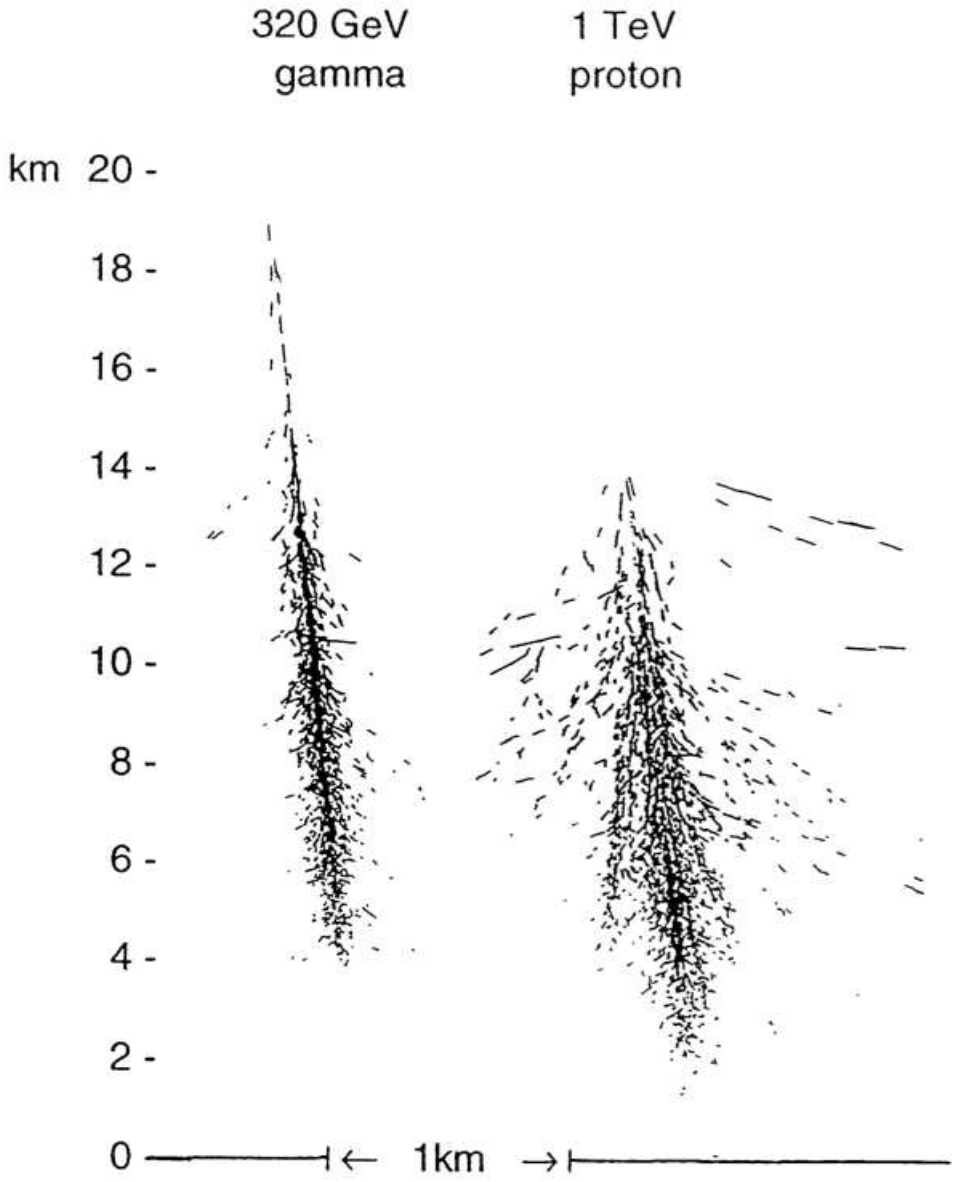

Figure 1.11. A comparison of a 320 GeV gamma ray EAS and a 1 TeV proton EAS. The horizontal scale has been magnified by a factor of five to show detail. Not all of the particle paths have been drawn to avoid saturation of the image. (Hillas 1996, with kind permission from Springer Science and Business Media)

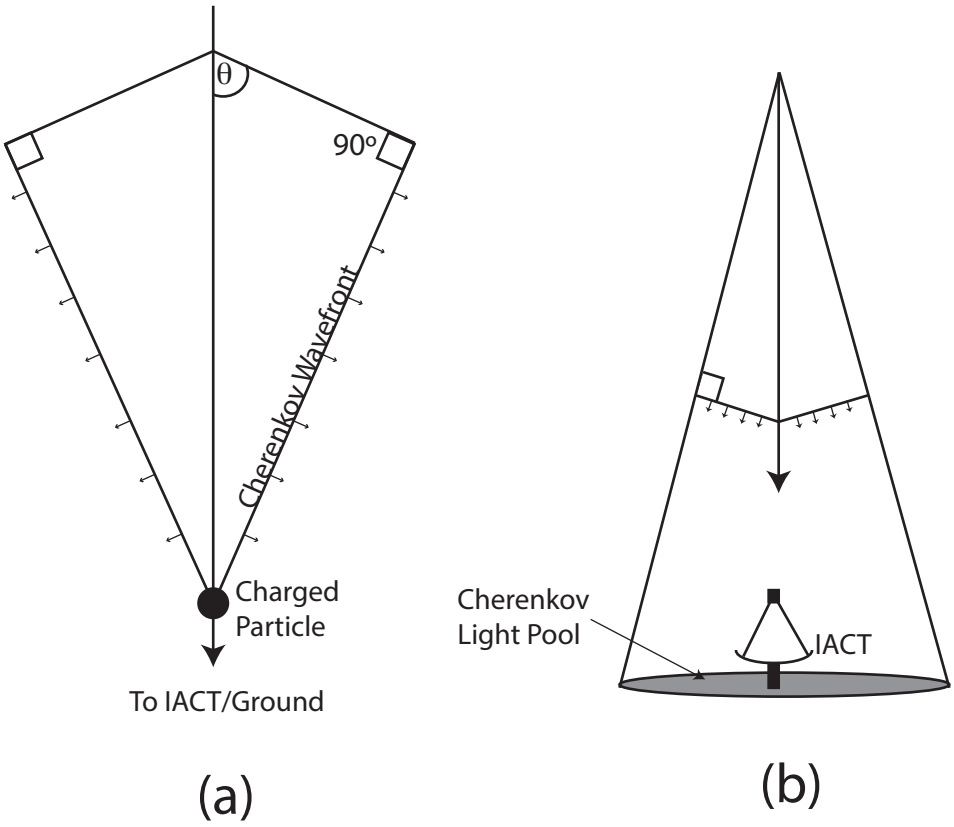

Figure 1.12. The wavefront of the Cherenkov radiation from an EAS. (a) shows the diagram of the Cherenkov light emitted by the charged particle. (b) shows the light cone that is swept out by the wave front of the Cherenkov light.

Cherenkov radiation wavelength peaks in the blue/UV light. The energy lost due to Cherenkov radiation is on the order of a few eV per photon. This amount of energy lost through Cherenkov radiation is less than a factor of 10^{-6} in total energy of the EAS.

1.3.2 Extensive Air Shower Arrays

EAS arrays are typically built of many small ground-based detectors such as the High Altitude Water Cherenkov (HAWC) array (Mostafa 2011). The ground-based detectors are water tanks with a few photomultiplier tubes inside the water to detect Cherenkov radiation emitted by particles passing through the water. Water has a higher index of refraction than air, allowing charged particles inside water to radiate Cherenkov radiation at a lower energy. Since the critical energy needed to create Cherenkov radiation in the water tanks is greater than a MeV, only an EAS with enough energy to produce MeV electrons at ground level will be detected. Arrival direction of the incoming EAS is determined from the timing of PMT pulses from the multiple water tanks.

The angular resolution of an EAS array is dependent upon the energy of the primary particle of the EAS. The highest energy particle's EAS triggers more detectors, which allows for a more accurate reconstruction of the arrival direction. For low energy primary particles ($E < 1TeV$), the angular resolution can be around one degree and for high energy particles ($E > 1TeV$), less than one-tenth of a degree.The duty cycle of an EAS array is much higher than IACT arrays. EAS arrays can be operated during the day when IACT arrays are inactive. The amount of light recorded by the PMTs is compared to Monte Carlo simulations to determine the energy of the primary particle of the EAS. The energy resolution for an EAS array, like HAWC (Tepe & the HAWC Collaboration 2012), is approximately between 30 and 50%.

CHAPTER 2

VERITAS

VERITAS is an array of four imaging atmospheric Cherenkov telescopes (IACTs) (Figure 2.1) located south of Tucson, Arizona, at the Fred Lawrence Whipple Observatory (Holder et al. 2006; Perkins et al. 2009). Each telescope is equipped with a 499 photomultiplier tube (PMT) camera with a 500 mega-samples per second flash ADC readout system. The optical reflector of each telescope is 12 meters in diameter and uses a Davies-Cotton mirror design (Davies & Cotton 1957). Each telescope has focal plane at a distance of approximately 12 meters. The field of view is approximately 3.5° in diameter.

2.1 Event Reconstruction

VERITAS detects the Cherenkov light images emitted by extensive air showers (EASs). Image parameters of the Cherenkov light image were first defined by Hillas (1996). The fitted Cherenkov image parameters are then compared with image parameters that are

Figure 2.1. The VERITAS telescopes. Credit: Steve Criswell, Smithsonian Astrophysical Observatory

derived from Monte Carlo simulations, and comparisons are made to distinguish gamma-ray showers from cosmic-ray/hadronic showers. The selection of events through Cherenkov image parameters are referred to as "cuts". Geometric parameters are applied to each event to calculate the arrival direction and the impact distance on the ground of the EAS. For each Cherenkov image, the number of photo electrons are calculated from the size of the pulse from the photomultiplier tubes that were triggered by the event. By comparing the image parameters and the total integrated pulse size of the Cherenkov image simulations, the energy of the primary particle is estimated.

2.1.1 Cherenkov Image Parameters

Standard image parameters defined by Hillas (1996) (Figure 2.2) are defined in Table 2.1. Image parameters are used to differentiate between a gamma ray induced EAS and a cosmic ray induced EAS. By comparing the RMS width, RMS length, and size of a shower to the impact distance of the core of the EAS on the ground, a determination can be made if the EAS was gamma ray initiated. The numerical value of the image parameters are determined from Monte Carlo simulations.

A set of Cherenkov images from a single VERITAS event is shown in Figure 2.3. Each image is fitted to an ellipse and several derived parameters are illustrated. The brightness of each image is dependent on the impact distance on the ground to each telescope.

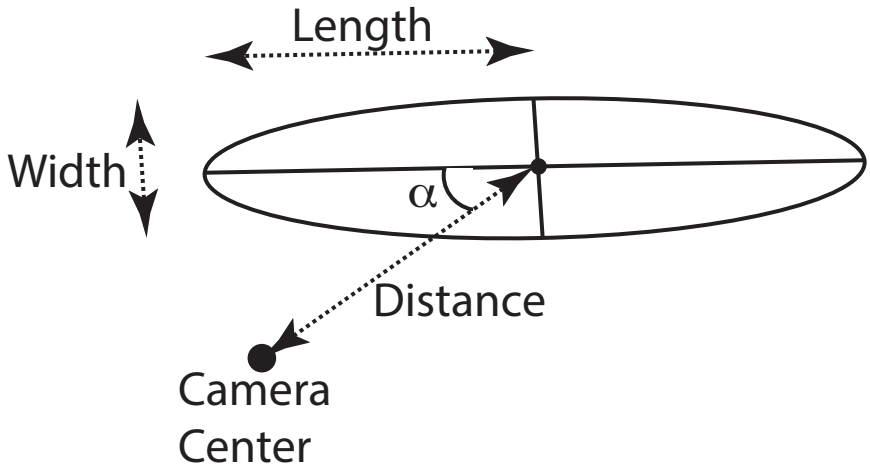

Figure 2.2. Hillas Parameters of an image as recorded by an IACT, adapted from Hillas (1996)

Table 2.1. Hillas image parameter definitions (Hillas 1996)

Parameter	Units	Definition
Size	Digital Counts	Total integrated signal from the PMTs after the night sky background has been cleaned away.
Length	Degrees (sky)	The RMS extent of the light along the major axis of the ellipse.
Width	Degrees (sky)	The RMS extent of the light along the minor axis of the ellipse.
Distance	Degrees (sky)	The distance from the centroid of the ellipse to the center of the camera.
α	Degrees	The angle between the line from the center of the camera to the centroid of the ellipse and the major axis.

2.2 Energy Range and Angular Resolution

The VERITAS IACTs detect gamma rays with energies from 100 GeV to greater than 30 TeV with an energy resolution of 15% at 1 TeV. The peak effective photon collection area is approximately $100,000 m^2\ sr$. The angular resolution is 0.1 degrees at 1 TeV with a location accuracy better than 50 arc seconds. VERITAS is capable of a 5σ detection of the Crab nebula (the standard candle for TeV astronomy) in 2 minutes and detection of a source of 1% Crab flux (10 $mCrab$) in less than 30 hours. VERITAS operates September through July, with an average yield of 750 hours of clear weather observation per year when the Moon is set, and 100 hours of clear weather observation per year when the Moon is above the horizon.

2.3 Observation Modes and Background Estimation

VERITAS observes sources in three different modes: ON-OFF, wobble, and orbit. ON-OFF mode requires two observation measurements. First, the ON data are taken with the telescopes pointed directly at the source of interest and following the source across the sky. OFF data are taken by slewing the telescopes to an off-source position at the same starting elevation and azimuth as the previous ON run, to closely match the light level and cosmic ray rate of the night sky, and following the same path across the sky as the ON run. ON-OFF mode allows observations of extended sources. Wobble mode data require only one observation per measurement. The telescopes observe the source across the sky with a fixed radial offset from the camera center in the cardinal directions. The off data for wobble

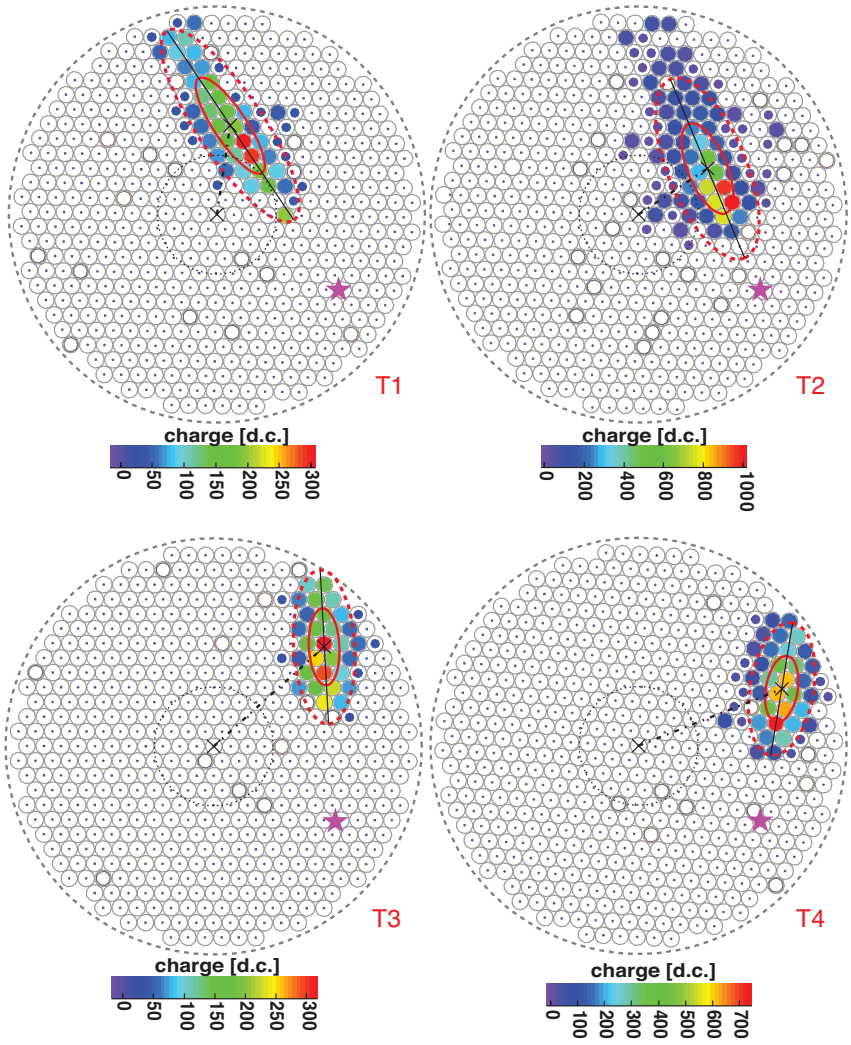

Figure 2.3. A single event as seen by the VERITAS telescopes with the fitted ellipse. The ellipse has a major axis equal to the RMS length, and the minor axis equal to the RMS width. The solid line is the major axis. The dashed line is the distance parameter. The X is the centroid of the camera and the Cherenkov image. The star is the reconstructed arrival directions of the primary particle.

mode are estimated from the same source observation, but at different locations in the field of view depending on analysis type.

For ON-OFF observations, regions in the camera are compared between the ON run and the OFF run. The ON run provides the signal and the OFF run provides the estimate for the background signal. If the durations of the ON and OFF run are different, then a normalization factor must be multiplied to the OFF run (Li & Ma 1983). The normalization

factor (α) is simply the ratio of the time spent on the source and the time spent off the source. If both the ON and the OFF run are the same duration, then the normalization factor is unity. The excess is then $N_{on} - \alpha \cdot N_{off}$, with N_{on} and N_{off} being the on and off counts. The significance is calculated using the likelihood ratio method as given by Li & Ma (1983).

Wobble mode observations are normally analyzed with the reflected region background method (Aharonian et al. 2001) or the ring background method (Berge et al. 2007). Wobble mode observations take advantage of the idea that the camera acceptance and the cosmic-ray background is isotropic. The camera field of view center during wobble mode observations of a source is offset from the source (R_{wobble}) in the cardinal directions, nominally from 0.5 to 0.7 degrees. This allows the background to be estimated at different locations in the field of view for the source (see Figure 2.4). For the reflected region background estimation, the background events are counted in regions that are at the same radial offset and size of the signal region. A normalization factor is applied to the background event count dependent only on the number of reflected regions used for the background estimation. The ring background estimates the background events by counting events within a ring surrounding the signal region. The ring uses an area approximately 10 times the signal region area. For the ring background estimation, an acceptance function of the camera must also be measured. The acceptance is a measure of the event reconstruction efficiencies versus the radius of the camera (Figure 2.5). Cherenkov images that occur near the edge of the camera are more difficult to reconstruct due to truncation of the shower image by the camera edge. For each event used in the ring background estimation, a weight is given to the background event to renormalize the background events as if they had been counted at a distance from the center of the FOV equal to the signal region. The size of the ring is also used in the calculation of the normalization and the acceptance function of the analysis. For the ring background, the normalization then becomes

$$\alpha = \frac{1}{A_{ring}} \cdot \sum_i \frac{1}{w_i}, \tag{2.1}$$

where A_{ring} is the area of the ring and w_i are the weights from the acceptance function for each event.

Orbit mode is a straightforward extension of the classic wobble mode. Instead of using a small set of source offsets, usually four in the cardinal directions, orbit mode observation maintains the telescope FOV center at a fixed radial offset, in right ascension

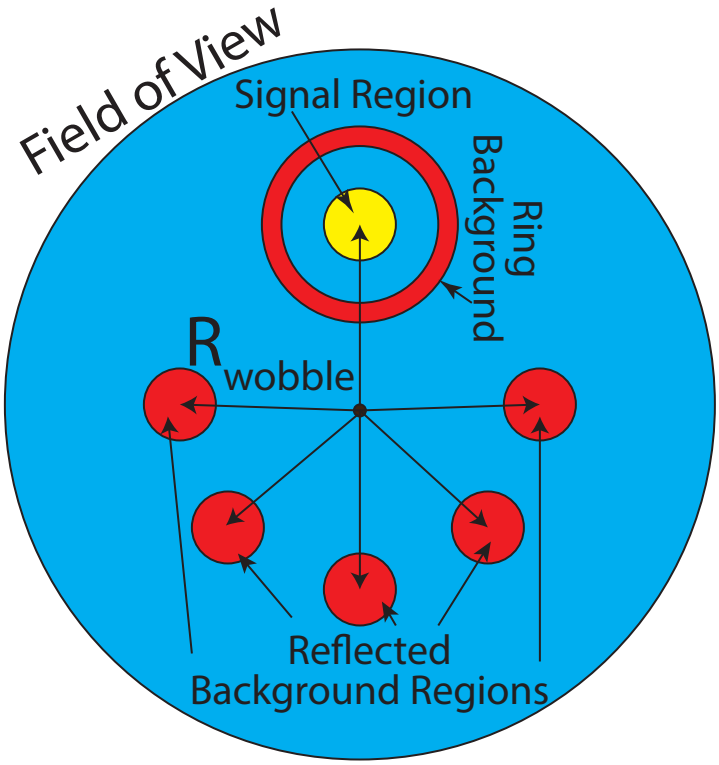

Figure 2.4. The reflected regions and ring background models. R_{wobble} is the radial offset of the signal region from the center of the camera.

and declination, from the source, while constantly changing the azimuth angle of the source in the FOV (Finnegan & the VERITAS Collaboration 2011). Standard wobble mode analysis methods can be applied to a data set taken in orbit mode. There are advantages to using orbit mode: orbit mode allows for longer observation without the wasted time in slewing the telescopes to the next cardinal position (approximately 2 minutes per data run), and it produces a radially symmetric exposure contour (Figures 2.6 and 2.7). The standard wobble mode observations create multiple steps in the exposure profile (see Figures 2.8 and 2.9).

To demonstrate that the orbit mode is a valid mode for observations, test runs were taken on the Crab nebula. A significant detection of greater than 25σ was achieved in a single 30-minute run with a gamma-ray rate of 10.0 ± 0.6 gamma rays per minute (see Figure 2.10). A wobble mode analysis was done on a set of four runs taken during the same time

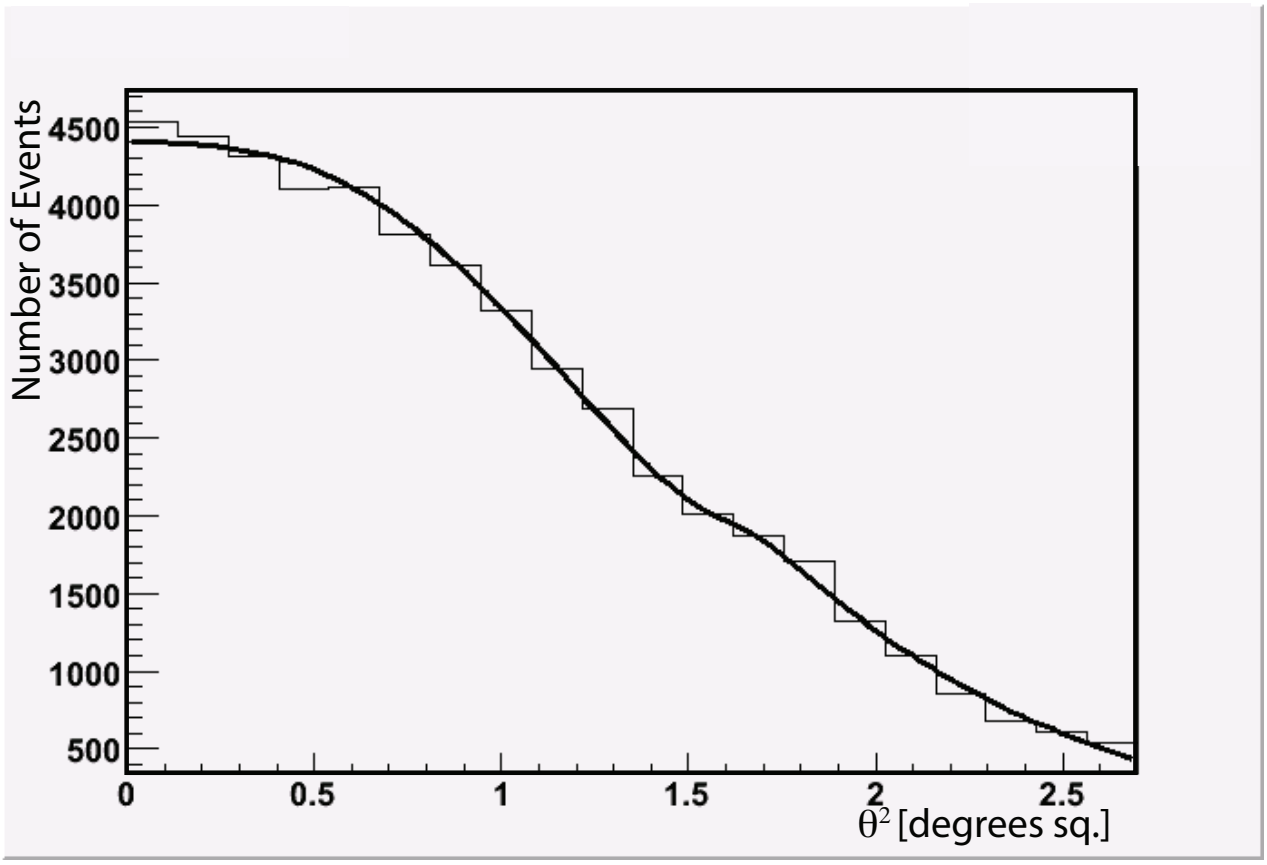

Figure 2.5. An example of the acceptance function of the camera. The number of events drops off towards the edge of the field of view. Cherenkov images that originate close to the edge of the field of view have shower images that are normally truncated at the edge, and become more difficult to reconstruct their geometric properties. The drop is caused by the inability to reconstruct events that fall near the edge of the field of view.

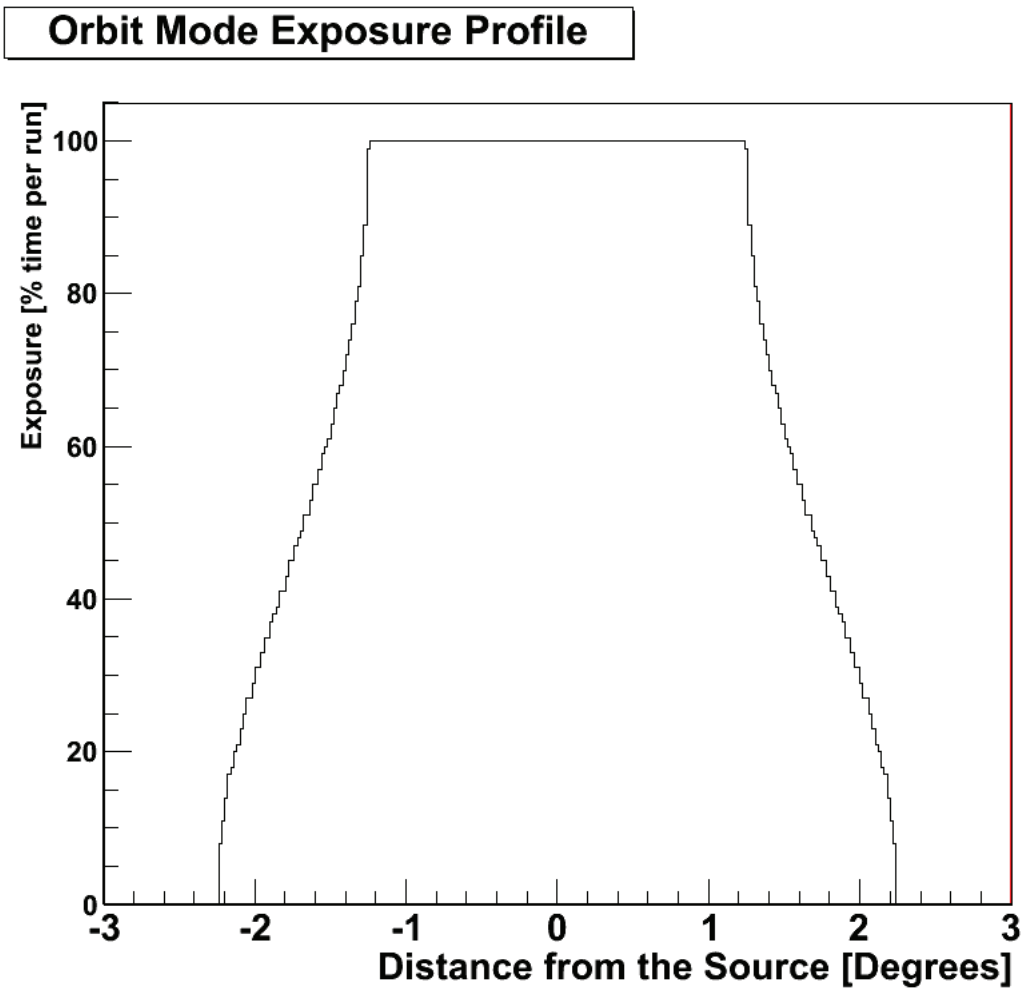

Figure 2.6. Orbit mode radial exposure profile. Orbit mode observation creates a radially symmetric exposure in all directions.

period with similar zenith angles and produced a gamma-ray rate of 9.1 ± 0.7 gamma rays per minute.

A point source is defined as a source with an emission region smaller than the point spread function of the telescopes. Wobble mode analysis, employing either reflected regions background or ring background estimation, works well with small diameter sources, particularly with point sources. If an astrophysical object's VHE emission area is large enough to overlap with both the signal area in the field of view and the background region, the

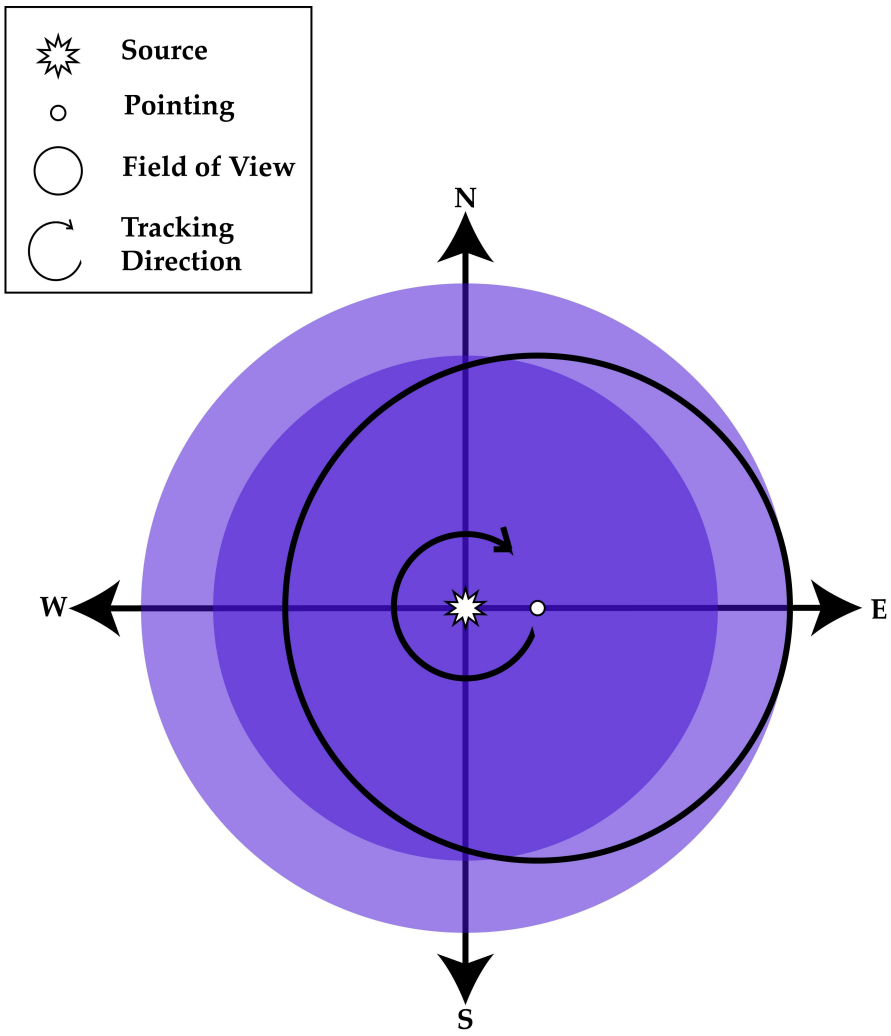

Figure 2.7. Two-dimensional exposure map of a single orbit mode run. The longer the exposure is, the darker the color in the map.

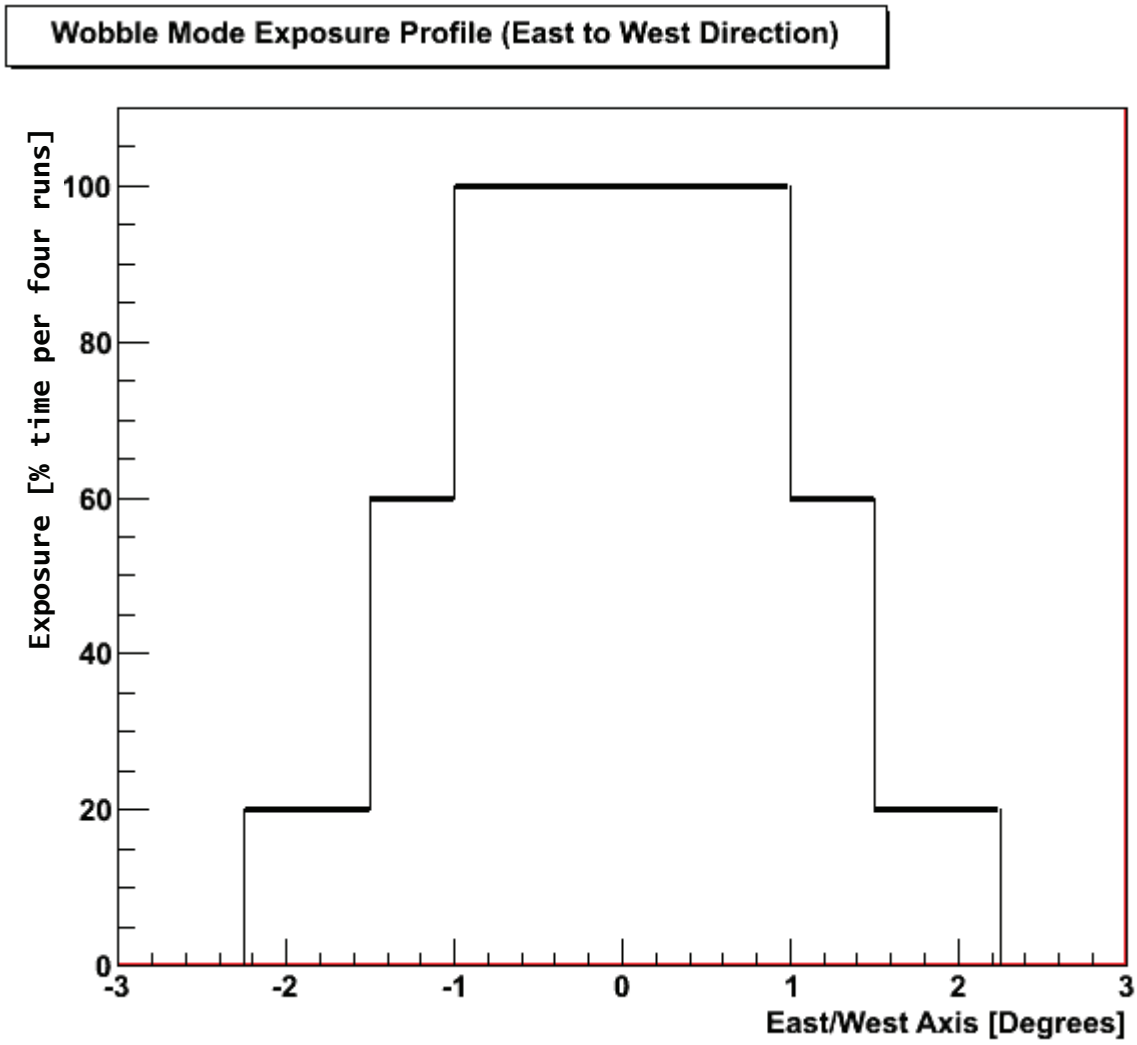

Figure 2.8. Woble mode radial exposure profile (East to West or North to South axis).

background will be overestimated. This overestimation is simply due to the excess counts from the source itself in the background regions. If the source covers the signal region and all the background regions, it is possible that no excess will be detected. Consequently, wobble mode analysis is generally unsuitable for extended ($\varnothing > 0.5^{\circ}$) source detections.

ON-OFF observations do not use the reflected regions or ring background method. Instead, analysis of ON-OFF observations uses direct comparison of regions in the FOV from the ON and OFF data runs. If it can be assumed that there are no sources in the

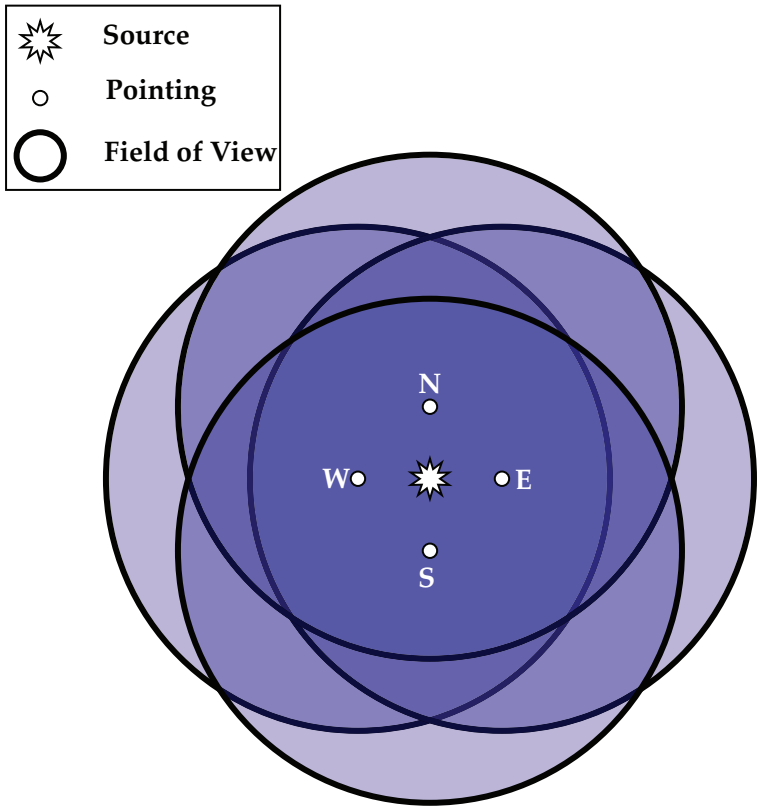

Figure 2.9. Two-dimensional exposure map of four wobble mode runs. The longer exposure is, the darker the color in the map.

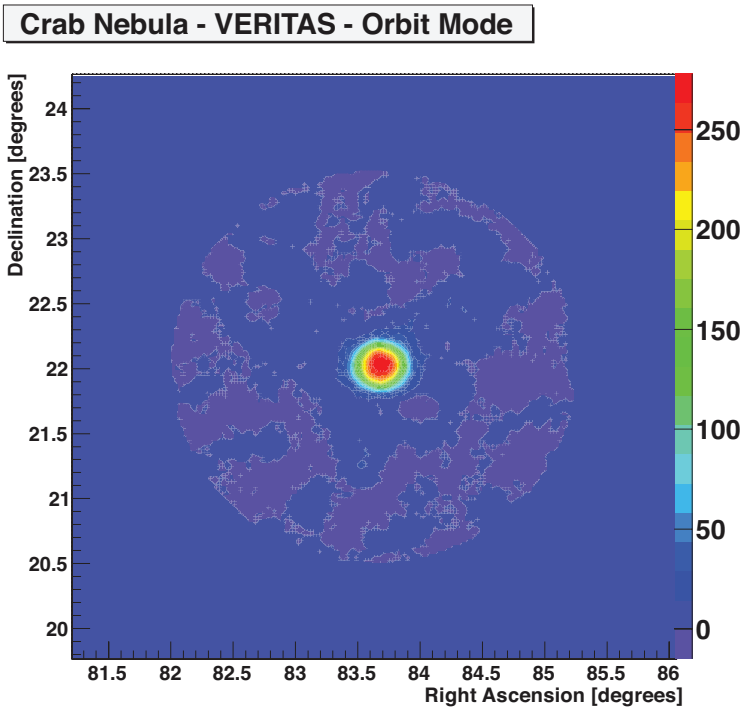

Figure 2.10. Excess map of the Crab Nebula from an orbit mode observation.

FOV of the OFF run, then the OFF run correctly estimates the background. ON-OFF observations allow a detection of an astrophysical source at very high energies with a radial extension approaching the size of the FOV.

A challenge for ON-OFF observations is systematic errors in the night sky background due to different external factors. More events trigger IACT arrays when the telescopes are pointed at low zenith angles (high elevation angles) due to a smaller amount of atmospheric attenuation versus large zenith angles. The night sky background (NSB) is dependent on the star field in the FOV and lights from neighboring cities. A higher trigger threshold is used when the NSB is high, causing less events to trigger the IACT array. It is important to match the zenith angle and NSB of each ON run to the OFF run to match the event rates. OFF observations are normally taken right after or before the ON run on the same night to match the conditions of the ON run.

Common to all observation modes is the binning method used to make maps of the regions. The resolution of the telescope is quantified by the point spread function (PSF): the 68% containment radius of a point source. The PSF then becomes the uncertainty of the actual event arrival direction. For every bin in the excess map, the excess counts are correlated for each bin. The N_{on} and N_{off} for each bin is the number of events that occurred inside the PSF radius centered at the bin center. The bins are correlated because the PSF covers more than a single bin.

2.3.1 ON-OFF Observations using Wobble Mode Observations

An analysis method that may prove useful for detecting extended objects is to match the source wobble mode data runs to other data runs (with a position external to the source run FOV) that have a similar NSB, zenith angle, azimuth angle, hardware, and weather conditions. The matched run used for the background must not have any excess gamma rays in the FOV. The wobble mode runs become the ON run, and the matched runs become the OFF run. The advantage of this is that no extra observation time was expended by the telescope array to observe the traditional OFF runs. This method was used in the detection of Vela-X by Aharonian et al. (2006a).

2.4 Observed Source Significance

The common method in gamma-ray astronomy for calculating the statistical significance σ is to use the significance formula from Li & Ma (1983, Equation 17).

$$\sigma = \sqrt{-2\ln\lambda} \tag{2.2}$$

$$\lambda = \left[\frac{1+\alpha}{\alpha}\left(\frac{N_{on}}{N_{on}+N_{off}}\right)\right]^{N_{on}}\left[(1+\alpha)\left(\frac{N_{off}}{N_{on}+N_{off}}\right)\right]^{N_{off}}. \tag{2.3}$$

Here N_{on} and N_{off} are the number of on and off counts in the signal and background, respectively, and α is the normalization factor. The above equation is derived from a likelihood ratio method. For the likelihood ratio, two hypotheses are tested. They are the null hypothesis, or what is the probability to observe $< N_s >=< N_{on} - \alpha N_{off} >= 0$, and the alternate hypothesis, the probability to observe $< N_s >\neq 0$. If N_{off} is greater than N_{on}, then by convention, the significance σ is negative; otherwise σ is positive.

If a new analysis is made on a previously analyzed set of data, a trial factor, that reduces the significance, must be accounted for in the significance of the source. Trial factors are also included if a source is detected in the FOV where the source was not expected to be found. This is known as a spatial trial factor. A simple method for calculating the spatial trial factors is by counting the number of spatial bins in the significance maps (A 2-dimensional map of the significances in the FOV). Since the bins are spatially correlated due to the PSF of the telescopes, counting bins for trial factors overestimates the number of trial factors. For a more accurate estimation of the spatial trial factors, one should include the PSF size in the calculation. Dividing the search region by the PSF gives a quick but slightly overestimated trial factor. The overestimation in the previous method comes from the fact that there are still some overlaps in the search region when using the area of the PSF. The trial factors are then folded into the significance by calculating the equivalent probability of the excess being pure random noise. The probability is multiplied by the trial factors, and then the equivalent significance is recalculated.

2.5 VERITAS and the Crab Nebula

The VERITAS IACT array is often calibrated using data collected while observing the standard candle in TeV astronomy, the Crab nebula. The Crab nebula is seen as a point source by VERITAS (see Figure 2.11) and has a measured flux of $(3.6 \pm 0.02) \times 10^{-11}\ TeV^{-1}cm^{-2}s^{-1}$ with a spectral index of -2.54 ± 0.05 (Celik & the VERITAS Col-

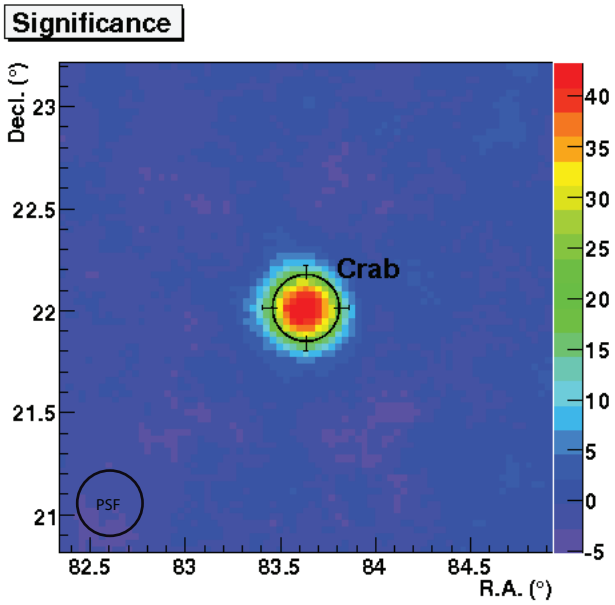

Figure 2.11. Significance map of the Crab Nebula. Black circle: 68% containment of the source.

laboration 2011). VERITAS can detect the Crab nebula at a 5σ level in approximately 2 minutes. The sensitivity of any VERITAS source detection depends on the source flux, usually measured in a ratio between the source flux and the Crab flux, or simply called "Crab units". Figure 2.12 shows the current VERITAS best-case scenario (good weather and high elevation angle) source sensitivity for a range of source fluxes from 0.003 to 3 Crab units. The angular resolution, or point spread function, is dependent on the energy of the primary gamma ray. Figure 2.13 shows the angular resolution, or the point spread function, as a function of energy for two data selection cut criteria. Standard data selection cuts try to minimize the number of cosmic-ray events that pass the cuts by setting the light yield threshold higher for each event. Soft cuts allow more gamma-ray events to pass the cuts by allowing lower light yields per event, which may be useful for detection of soft-spectra sources (spectra that are steeper than the cosmic ray spectrum).

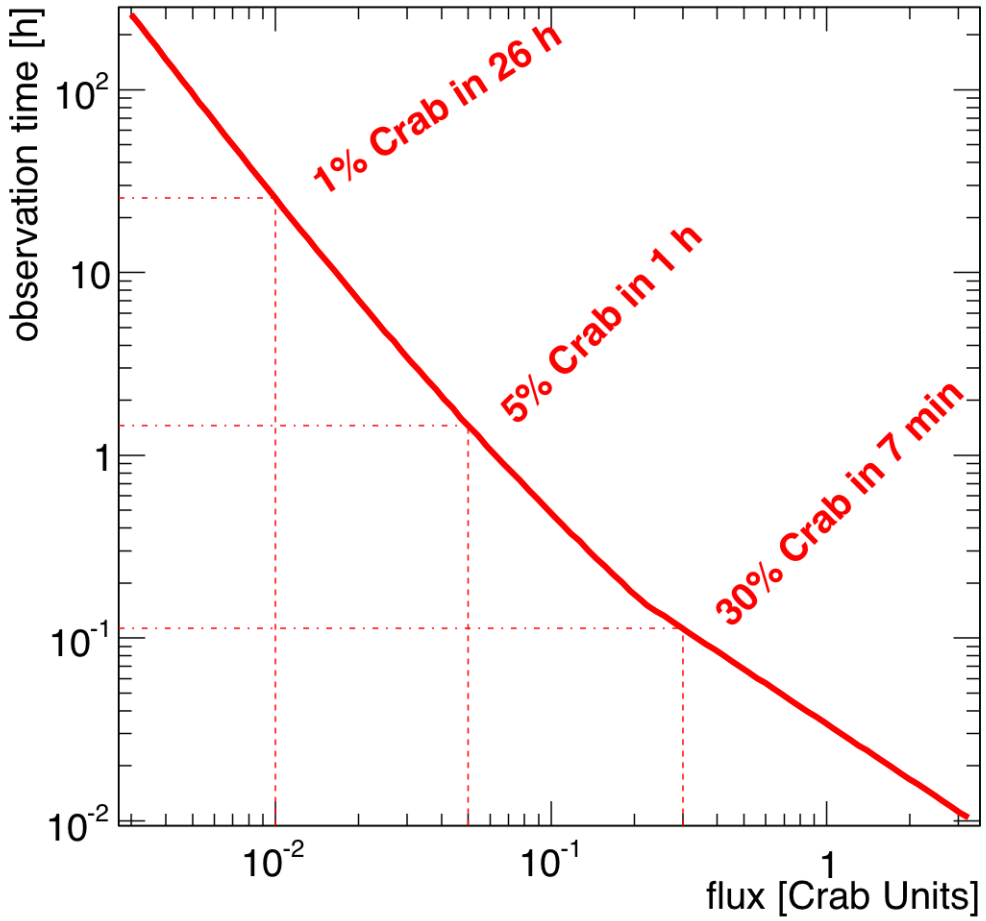

Figure 2.12. The VERITAS sensitivity: the observation time as a function of flux (Crab Units). Credit: Gernot Maier for the VERITAS Collaboration, Smithsonian Astrophysical Observatory

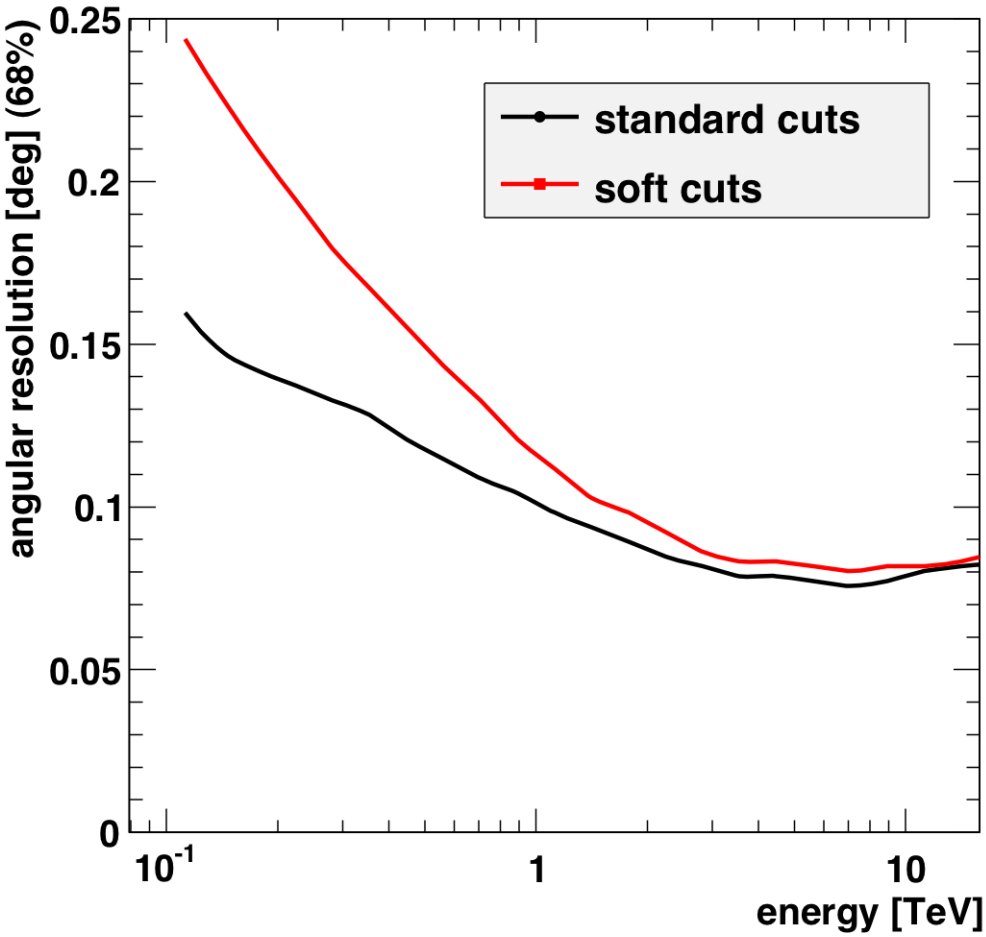

Figure 2.13. The angular resolution of VERITAS observations as a function of the primary gamma ray's energy. The black line is results from the standard data selection cuts, and the red line is from the soft cuts.

CHAPTER 3

GEMINGA

Geminga is the remnant of a large supernova which occurred approximately 10^5 years ago in an optically obscured region of the galactic plane. The Geminga pulsar (right ascension $06^h33^m54.15^s$, declination $+17°46'12.99''$, epoch J2000.0) is an isolated neutron star from the supernova remnant of the massive progenitor star. Geminga is a unique laboratory: it was the first neutron star and astronomical object that was discovered through gamma-ray observations, and has been one of the most studied high energy astrophysical sources since its discovery.

3.1 1970s - 1980s

The Small Astronomy Satellite 2 (SAS-2) space-based gamma-ray observatory, launched in 1972, first reported high energy gamma-rays from the direction of Geminga in 1975 (Fichtel et al. 1975). The exact origin of the high energy emission from the direction of Geminga from the SAS-2 data, was not given at this time. Fichtel reported that the emission region came from "a region a few degrees north of the galactic plane around 190° to 195°", in the galactic coordinate system. The poor localization of the excess helped fuel ideas (Abdulwahab & Morrison 1978) that Geminga, as seen in the SAS-2 data, was an extended or diffuse object. Thompson et al. (1977) reported on the SAS-2 results of the galaxy anticenter region, and found that the excess region was consistent with a point source located at $l = 194.9° \pm 1.5°$, $b = 4.9° \pm 2.2°$, essentially eliminating the idea that the excess was extended.

In 1975, the European Space Agency (ESA) launched the COS-B satelite with a gamma-ray observatory onboard. Hermsen et al. (1977), reported 13 high energy gamma-ray sources detected from the COS-B gamma-ray data. One of the 13 was the point source CG195+4, with galactic coordinates of $195.9 \pm 1.0l^{ii}, +4.5 \pm 0.5b^{II}$ and a relative flux similar to the Crab pulsar, associated with the SAS-2 high energy emission region.

In 1978, NASA launched the High Energy Astrophysical Observatory 2 (HEAO-2), renamed the Einstein satellite after launch. The Einstein satellite detected thousands of X-ray sources. Five X-ray sources were detected in the error box of the COS-B CG195+4 source. Four of the X-ray sources had very low flux levels. One of those sources, 1E 0630+178, had a high flux level and was therefore attributed to the COS-B gamma-ray source. Bignami et al. (1983) were able to conclude that the high energy X-rays were coming from a neutron star. Bignami also searched for pulsed emission from the Einstein Geminga observations, but none was found. Typically, neutron stars are first detected through ground-based radio observations. Because no radio detections had been made in the 1E 0630+178 region, Bignami cleverly named the source Geminga, which is a contraction of two words *Gemin*i, for the constellation of Gemini where the neutron star is located, and *ga*mma-ray."Geminga" means "does not exist" or "it's not there" in Milanese dialect (Bignami et al. 1983).

3.2 1990s - Present

In 1990, the Röntgen Satellite (ROSAT) with an X-ray observatory on board was launched. ROSAT was a cooperative program between three countries, Germany, the United States, and the United Kingdom. Halpern & Holt (1992) analyzed the Geminga data from the ROSAT satellite and discovered X-ray pulsations with a period of 0.237 s (see Figure 3.1). This confirmed suspicions that Geminga was a pulsating star (pulsar).

The EGRET gamma-ray instrument onboard the Compton Gamma-Ray Observatory, launched by NASA, observed the Geminga region from April to June of 1991 (Bertsch et al. 1992). Bertsch et al. (1992) were able to detect pulsed emission from Geminga with shorter observation exposures than previous instruments. This enabled them to divide the data into 5-day increments and to precisely measure a period for each of those increments. Because of the high precision of the measured periods for the 5-day increments, a period derivative was found of $(11.4 \pm 1.7) \times 10^{-15}\ s/s$. A characteristic age of Geminga of approximately 3×10^5 years can be calculated from the period derivative.

The European Space Agency's X-ray multi-mirrored space observatory (XMM-Newton) has been in service since December 1999. XMM-Newton was the first X-ray telescope to provide high resolution images of the Geminga pulsar and surrounding region (Figure 3.2). Caraveo et al. (2004) discovered what appears to be twin tails surrounding the pulsar. Caraveo hypothesized that the tails were from the bow shock created from the motion of

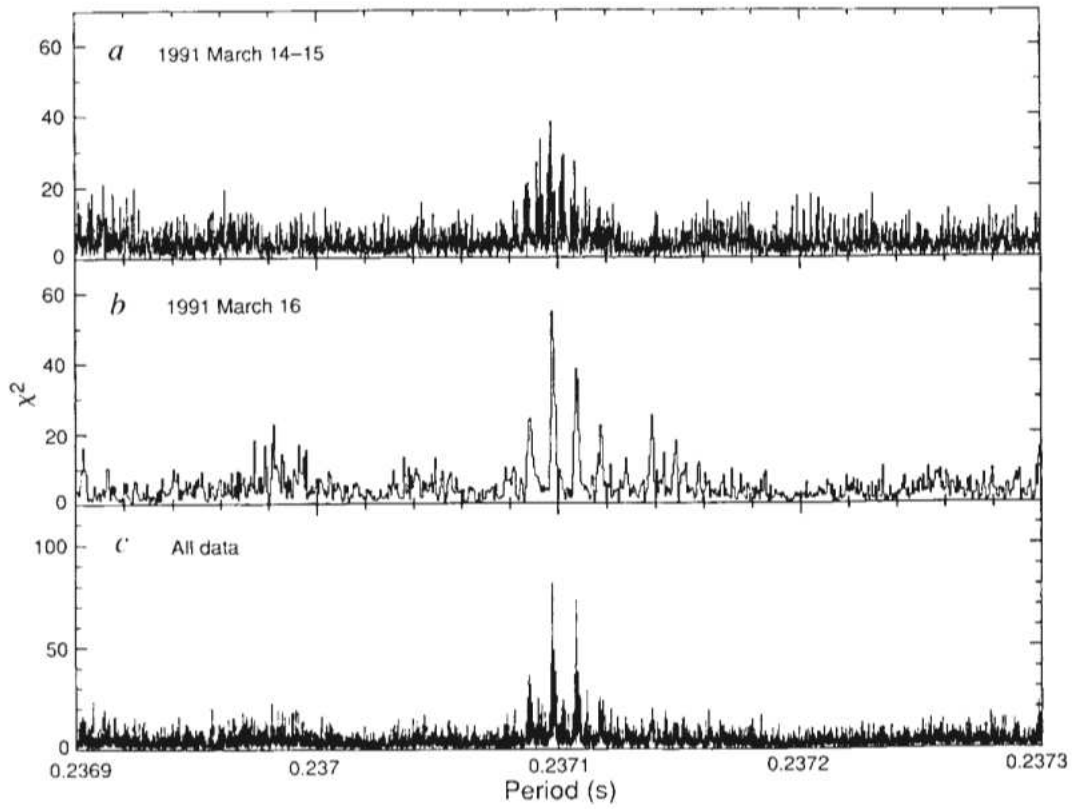

Figure 3.1. The ROSAT periodograms of Geminga data. Reprinted by permission from Macmillan Publishers Ltd: Nature (Halpern & Holt 1992)

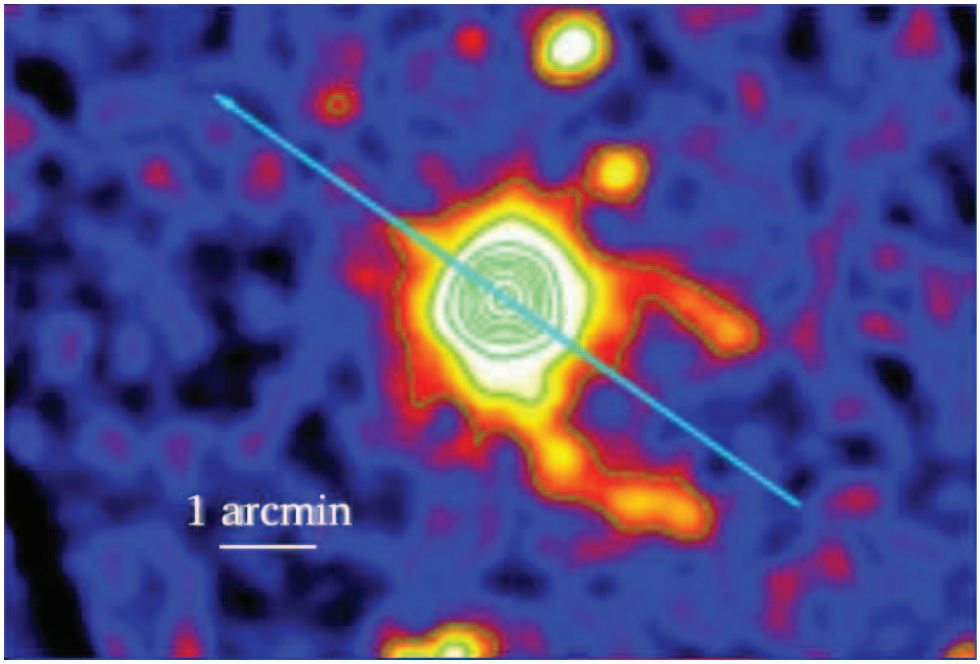

Figure 3.2. XMM-Newton image of Geminga (top) showing the discovery of twin tails. The motion of Geminga across the sky is indicated, showing the trailing tails of the neutron star. Image courtesy of P.A. Caraveo (INAF/IASF), Milan and ESA.

Geminga, and that the tails themselves were seen due to the limb darkening affect.

NASA's Chandra X-ray observatory, launched in 1999, produces high resolution X-ray images. Pavlov et al. (2006 & 2010) reported on the data taken of the Geminga pulsar and observed the tails as seen by Caraveo et al. (2004) with an additional axial tail. Pavlov also noted of the evidence of variability of the X-ray emission (Pavlov et al. 2010).

The Milagro experiment (Abdo et al. 2007) reported an angular extended TeV emission region C3, which was positionally consistent with Geminga. They reported an angular extension of the emission of $2.8° \pm 0.89°$, with an upper limit on the TeV flux of approximately 10% of the Crab nebula, assuming the emission was from a point source. With the earlier detection of an X-ray PWN from the Chandra instrument, it is assumed that the excess as seen by Milagro is also due to the PWN of Geminga. Milagro recently updated an analysis of Geminga (Abdo et al. 2009d) with improved absolute flux estimates at 35 TeV.

The Fermi Large Area Telescope (Fermi LAT) on board the Fermi space-based observatory, launched by NASA, has been in operation since 2008. The Geminga pulsar has been detected by the Fermi LAT (Abdo et al. 2010b), and is the second brightest source in the GeV energy range as seen by the Fermi LAT (the brightest source is the VELA pulsar, and after Geminga is the Crab pulsar). Spectral studies done with the Fermi LAT data have shown that GeV emission occurs at all rotational phases (Abdo et al. 2010b). Figure 3.3 shows the phased average spectral energy distribution (Abdo et al. 2010b) of the Geminga pulsar with the 35 TeV Milagro point (Abdo et al. 2009d).

Caraveo et al. (1996) and Faherty et al. (2007) have measured the parallax distance to the optically faint ($m_v \sim 25$) Geminga neutron star using the Hubble Space Telescope's (HST). Caraveo et al. reported a distance of 157 pc (+54, -34) using HST's Wide Field and Planetary Camera 2 (WFPC2). Using HST's Wide Field Camera (WFC), Faherty

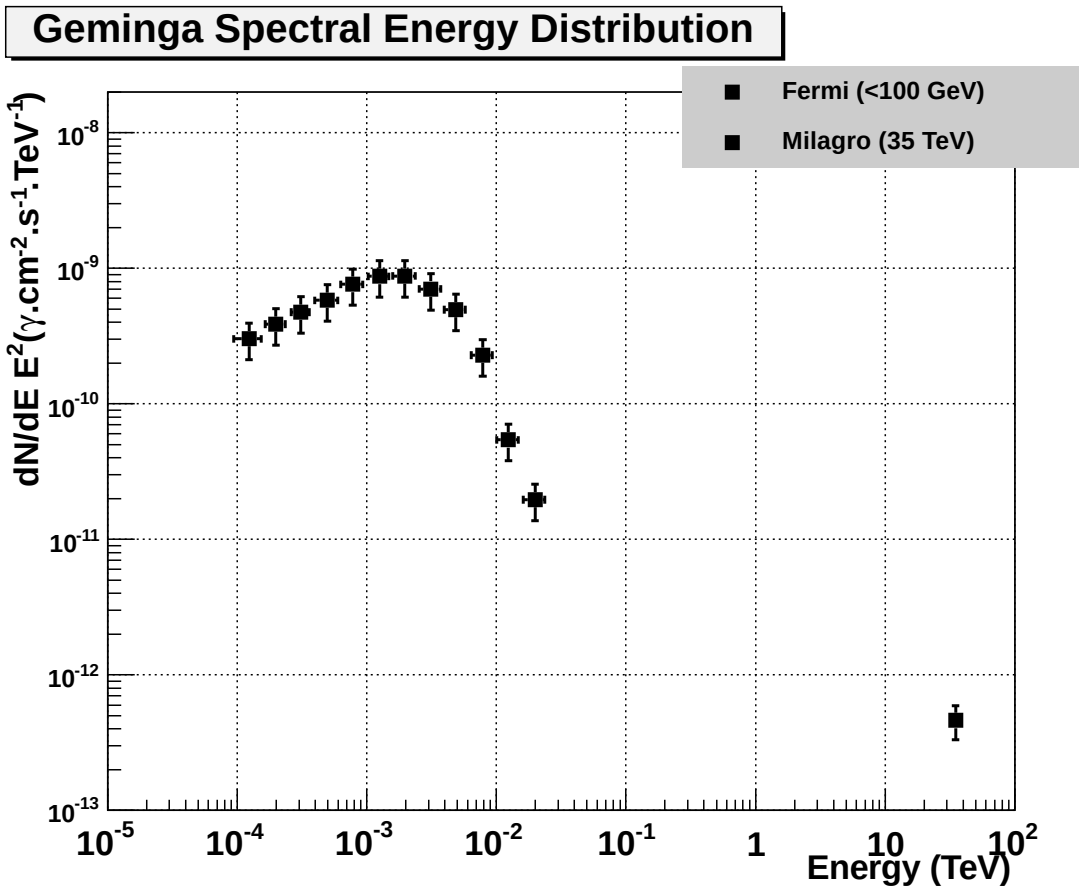

Figure 3.3. Fermi and Milagro spectral energy distribution of Geminga

et al. measured a distance of 250 pc (+120, -62), a result greater than 60% larger than previously measured. The proper motion of Geminga of 0.17 arcsec per year was measured with ground-based optical telescopes by Bignami et al. (1993).

Kassim & Lazio (1999) have given a report on the many radio observations of Geminga. There has been no significant radio detection of the Geminga pulsar. Typically, pulsars are discovered first through radio observations, for many of them are radio bright. Geminga was the first pulsar to be discovered through X-ray/gamma-ray observations, but would not be the last. Abdo et al. (2009a) reported on 16 new pulsars discovered with the Fermi LAT that added a new generation of radio-quiet pulsars.

Two previous generation IACT telescopes, Hegra and Whipple, also observed the region surrounding Geminga. The Hegra collaboration reported an upper limit (3σ) flux of 13% of the Crab flux (Aharonian et al. 1999). The Whipple collaboration reported a 3σ upper limit flux of $8.8 \times 10^{-12} cm^{-2} s^{-1}$ ($E > 0.5\ TeV$) or approximately 12.5% of the Crab flux.

The three brightest (in GeV energies) pulsars' characteristics are summarized in Table 3.1. The spin-down luminosities were calculated using a radius of 10 kilometers for the neutron star, and a mass of $1.4 M_{\odot}$.

Because of the close distance, others have suggested that the Geminga SNR/pulsar is the progenitor of a large-scale cosmic-ray anisotropy (Salvati & Sacco 2008). The characteristic age (3×10^5 years) along with the measured high energy emission make Geminga an interesting target for studying older aged pulsars. A possible confirmation of the age of Geminga has come from isotope sampling in ice cores (Ellis et al. 1996). Until recently, no detection of a nebula component of Geminga had been accomplished. The Milagro detection showed an extremely extended object, roughly five times the width of the Moon. This was the first evidence that there could be a PWN associated with the pulsar. An alternate theory of the extended emission in the region of Geminga, as seen by Milagro, was produced by Yüksel et al. (2009). They theorized that the high energy emission from Geminga could be a clue to the origin of the electron/positron excess as first seen by ATIC (Chang et al. 2008), due to the excess electrons that would interact with the cosmic microwave background photons through inverse Compton scattering.

---

[1]The flux above 100 MeV obtained by integrating the fitted phase average spectrum from the Fermi data.

[2]Statistical and systematic errors added in quadrature.

Table 3.1. A Comparison of Vela, Geminga, and the Crab pulsars. The spin-down luminosity is calculated from the pulsar energetics (see Section 1.2.1.2). References: [1]: Abdo et al. (2009b), [2]: Caraveo et al. (2001) , [3]: Abdo et al. (2010a), [4]: Kaplan et al. (2008), [5]: Abdo et al. (2010b), [6]: Faherty et al. (2007)

Pulsar	Characteristic Age ($years$)	Pulsar Period (s)	Period Derivative ($s\ s^{-1}$)	Distance (pc)
Vela [1],[2]	1.2×10^4	0.089	-1.24×10^{-13}	294^{+50}_{-76}
Geminga [5],[6]	3×10^5	0.237	-1.1×10^{-14}	250^{120}_{-62}
Crab [3],[4]	1240	0.033	-4.2×10^{-13}	2000 ± 500

Pulsar	Flux > 100 MeV ($10^{-6} cm^{-2} s^{-1}$)	$\dot{E}$ (Spin Down Luminosity)	B_{min} Near Surface (Gauss)	$L > 100MeV$ (Luminosity)
Vela	~ 9.35 [1]	$7.63 \times 10^{29} W$	3.4×10^{12}	$1.5 \times 10^{27} W$
Geminga	4.14 ± 0.32[2]	$3.26 \times 10^{27} W$	1.6×10^{12}	$5.0 \times 10^{26} W$
Crab	2.09 ± 0.18[2]	$5.1 \times 10^{31} W$	3.8×10^{12}	$1.5 \times 10^{28} W$

Pulsar	$L/\dot{E}$
Vela	0.002
Geminga	0.007
Crab	0.0003

CHAPTER 4

ANALYSIS OF THE VERITAS GEMINGA DATA

The analysis of Geminga was performed with the GrISU analsysis package (Le Bohec 2009). GrISU is a gamma ray simulation program developed at Grinnell College, Iowa State University, and the University of Utah. Additional GrISU subprograms for VERITAS data analysis were developed at the University of Utah. In particular, a program called datareader was developed to analyze the EAS recorded by VERITAS, and to produce sky maps of reconstructed events.

VERITAS has observed Geminga during three past observing seasons (2007, 2010, 2011). A point source search was initiated in 2007 with 15 hours of wobble mode observations. The wobble mode data had an offset of 0.5 degrees in the cardinal directions. An extended source search was initiated in 2010 with 30 hours of ON-OFF data, and continued with 15 hours of ON data in the 2011/2012 season.

4.1 Point Source Search

The 2007 wobble mode observations were analyzed using a point source analysis using the reflected region background method (Aharonian et al. 2001) and the ring background method (Berge et al. 2007). Significance is determined using the likelihood ratio method from Li & Ma (1983). No significant detection of a point source was obtained in the Geminga region. The 99% flux confidence level limit (Helene, O. 1983) for a steady source analysis with energies above 300 GeV is $< 2 \times 10^{-12} cm^{-2} s^{-1}$. A similar analysis was done on the Crab nebula, and resulted in a significant detection of 8.7 ± 0.4 gamma rays per minute at a flux of 1 TeV of 3.49 ± 0.19 $photons\ Tev^{-1} m^{-2} s^{-1}$.

A periodicity analysis was done on the 2007 data (Kieda 2008). The arrival times of each event, after barycentric corrections were applied, were compared to the ephemeris of

Geminga based on the XMM-Newton, ASCA, and EGRET data (Jackson & Halpern 2005). No significant detection of a pulsed point source at the Geminga pulsar location was found. The 99% flux confidence level limit of the pulsed point source analysis with energies greater than 200 GeV is $0.8 - 1.0 \times 10^{-12} cm^{-2} s^{-1}$.

4.2 Extended Source Analysis

The 2007 and 2009 Milagro results (Abdo et al. 2007, 2009d) showed the VHE emission of Geminga to be highly extended with a diameter ($\varnothing$) between 1.7° and 3.3°. The extended size of Geminga as seen by Milagro at 3.3° would fill the entire field of view of the VERITAS telescopes, making background estimation techniques such as the reflected region and ring background method unusable.

4.2.1 2007 Data

A new ON-OFF analysis was started on the 2007 wobble data using the technique described in Section 2.3.1 and with the data selection criteria cuts described in Table 4.1. The data were analyzed and an excess was found with a pretrials significance of greater than 5σ. In the event that no source is detected in the field of view, a histogram of the significances of each bin in the two-dimensional significance map should reveal a distribution similar to a gaussian distribution (Li & Ma 1983). The theoretical significance distribution should be centered at zero and the width of the distribution should be one. The observed significance distribution shows an offset in the mean of the distribution and the width is

Table 4.1. Data selection criteria cuts for the 2007 Geminga data. T_{on} and T_{off} are the duration of the total observations for the ON and OFF off runs, respectively.

Number of ON Hours (hours)	Integration Region (degrees sq.)	Minimum Number of PMTs	Minimum Digital Counts	Width Interval (degrees)	Impact Distance/ Length (m/degrees)
14.9	0.08	2	500	0.045-0.09	1.8-8.0

Average Zenith Angle (ON/OFF)	α (T_{on}/T_{off})
17.6°/21.1°	0.9938

broader than one (see Figure 4.1). Figures 4.2 and 4.3 show the significance and excess of the Geminga region for the 2007 data.

4.2.2 Significance Distributions

The offset in the mean of the distribution and the width of the distribution were studied by randomly generating ON-OFF event counts from a Poisson distribution. The study was performed to determine the affect an underestimated background and an extended source

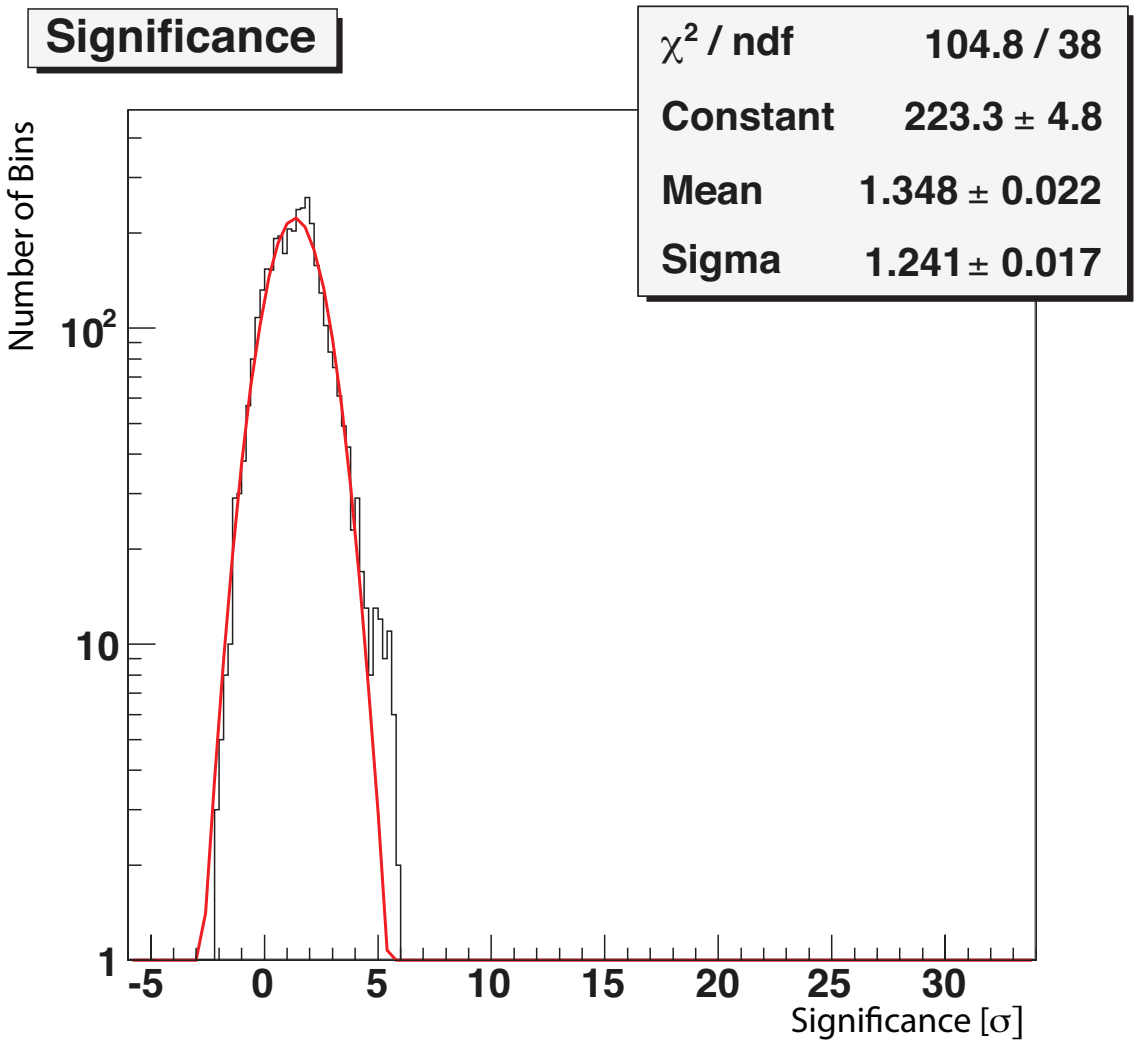

Figure 4.1. Pretrials significance distribution of the 2007 wobble data shows an offset of the mean, which is normally centered at zero, and a broadening of the distribution width.

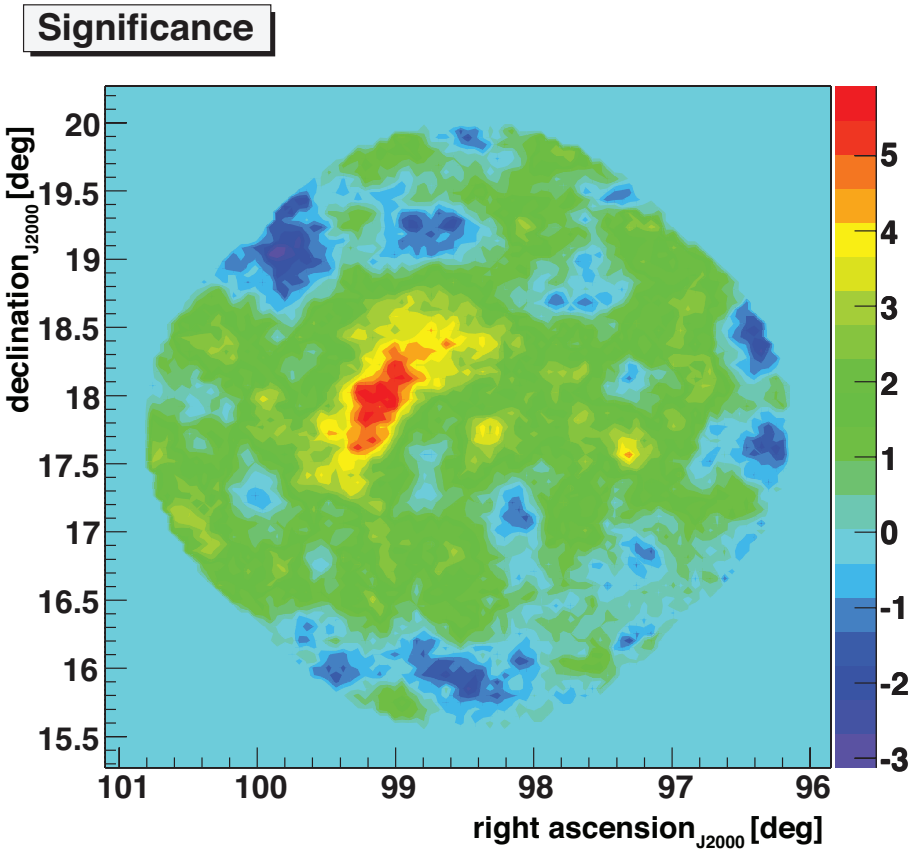

Figure 4.2. The significance of each bin for the 2007 data in the Geminga region.

in the FOV has on the significance distribution. The number of ON events and OFF events were randomly chosen from a Poisson distribution. The significance was determined from the significance calculation from Li & Ma (1983).

There were four parameters, a source in the FOV, the source extension, the source strength, and the background level, that were varied. Figure 4.4 shows an example of the results, and Table 4.2 shows a summary of the various outcomes to the distribution mean and width. The general trend is that for an extended source, the distribution width is extended, but not for a point source. The mean of the distribution is greater than zero when the background is underestimated. The background was underestimated by adjusting the mean values of the Poisson distributions so that the ON distribution was greater than the OFF distribution (Figure 4.5).

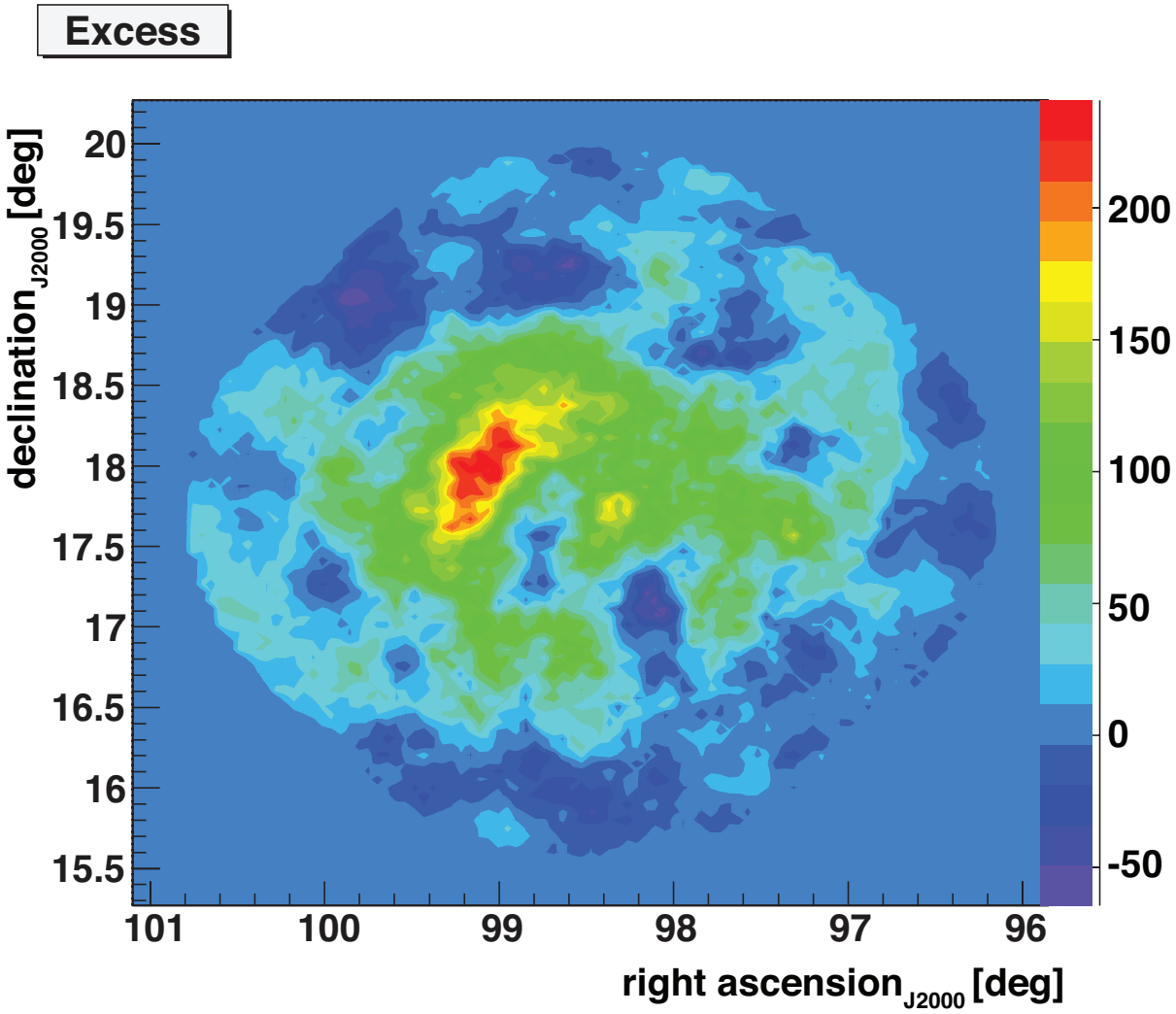

Figure 4.3. The excess events for each bin for the 2007 data in the Geminga region.

4.2.3 Spectra Analysis

A spectral study was done by selecting events that had a central impact distance less than $130m/\cos(z)$ to the telescopes, where z is the zenith angle of the observations, and comparing the total integrated FADC digital counts (size) of the events in the ON runs and the events in the OFF runs. The central impact distance cut was employed to minimize corrections to the spectral index due to energy dependent detection efficiency biases.

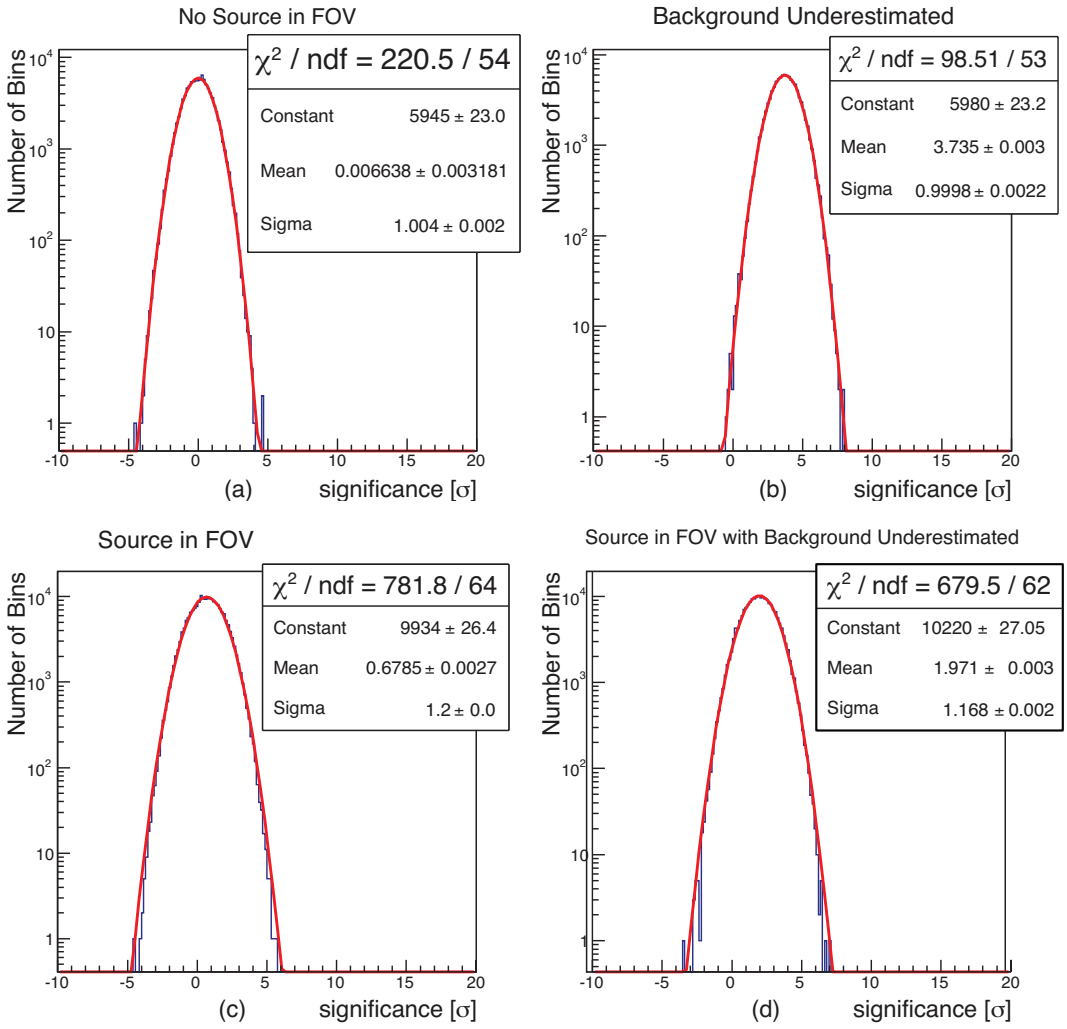

Figure 4.4. Histograms of the significances for each map bin of a simulated gamma-ray sky map. Figure (a) is a nondetected source distribution, (b) underestimated background with no source, (c) a highly extended ($\varnothing = FOV$) weak source with a properly estimated background, (d) and highly extended weak source with the background underestimated.

A ON-OFF spectral analysis was performed on a small sample of VERITAS Crab nebula data. The cuts applied during the extended source Geminga analysis were also applied to the Crab data. A slightly greater than 5σ result was achieved. The ON events (with a weight of one for each event) and the OFF events (with a weight of minus one for each event) were filled into a histogram. A power-law function, $A \cdot E^{\Gamma}$, was fitted to the events, and a value for Γ was found of -2.4 ± 0.6 with a reduced $\chi^2 = 0.8$ (Figure 4.6). The nominal Crab nebula spectral index is -2.5.

Table 4.2. Table summary of the distribution study of significances in the FOV

Source in Fov	Source Extension	Source Strength	Background Underestimated	Distribution Mean	Distribution Width	Figure
no	-	-	no	0.007 ± 0.003	1.004 ± 0.002	4.4(a)
no	-	-	yes	3.735 ± 0.003	0.999 ± 0.002	4.4(b)
yes	$\varnothing = FOV$	weak	no	0.679 ± 0.003	1.2 ± 0.1	4.4(c)
yes	$\varnothing = FOV$	weak	yes	1.971 ± 0.003	1.168 ± 0.002	4.4(d)
yes	$\varnothing = \frac{1}{10}FOV$	strong	yes	3.887 ± 0.004	1.105 ± 0.003	4.5(a)
yes	$\varnothing = \frac{1}{100}FOV$	strong	yes	3.736 ± 0.003	1.001 ± 0.002	4.5(b)

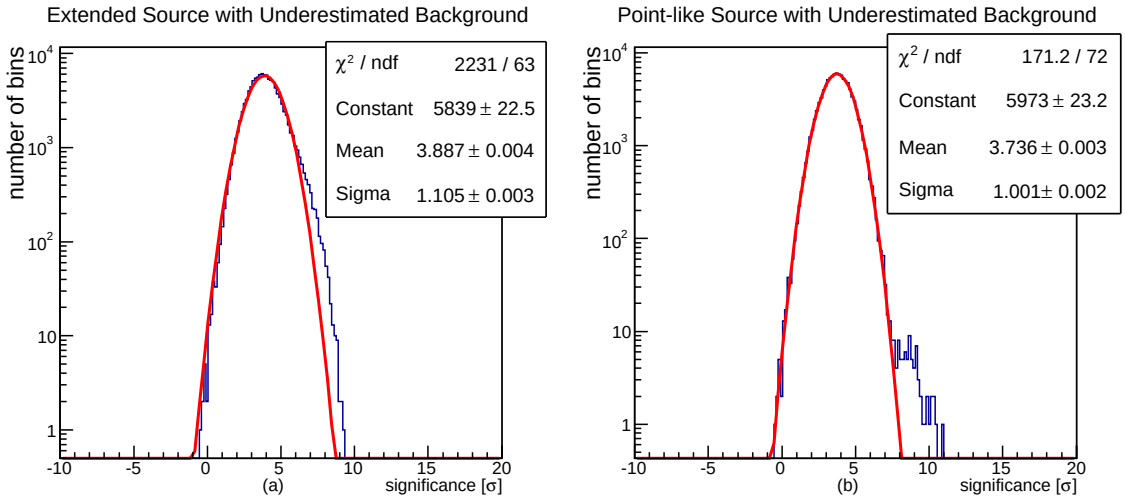

Figure 4.5. Simulated significance histograms of an extended and point-like source. Figure (a) shows the extended source and figure (b) shows the point-like source. The red line is the gaussian fit to the distribution and the blue is the simulated data.

The same spectral analysis procedure was performed on the 2007 VERITAS Geminga data (Figure 4.7). A spectral index of $\Gamma = -2.5 \pm 0.2$ was found with a reduced $\chi^2 \sim 1$.

4.2.4 2010 Data

Observations of Geminga were made during the 2010/2011 observation season with the data selection criteria cuts described in Table 4.3. The observation mode was ON-OFF. The 2010 data set was analyzed using the ON-OFF analysis with the same cuts as the extended 2007 data analysis. Figure 4.8 shows the excess gamma rays observed in this analysis. A

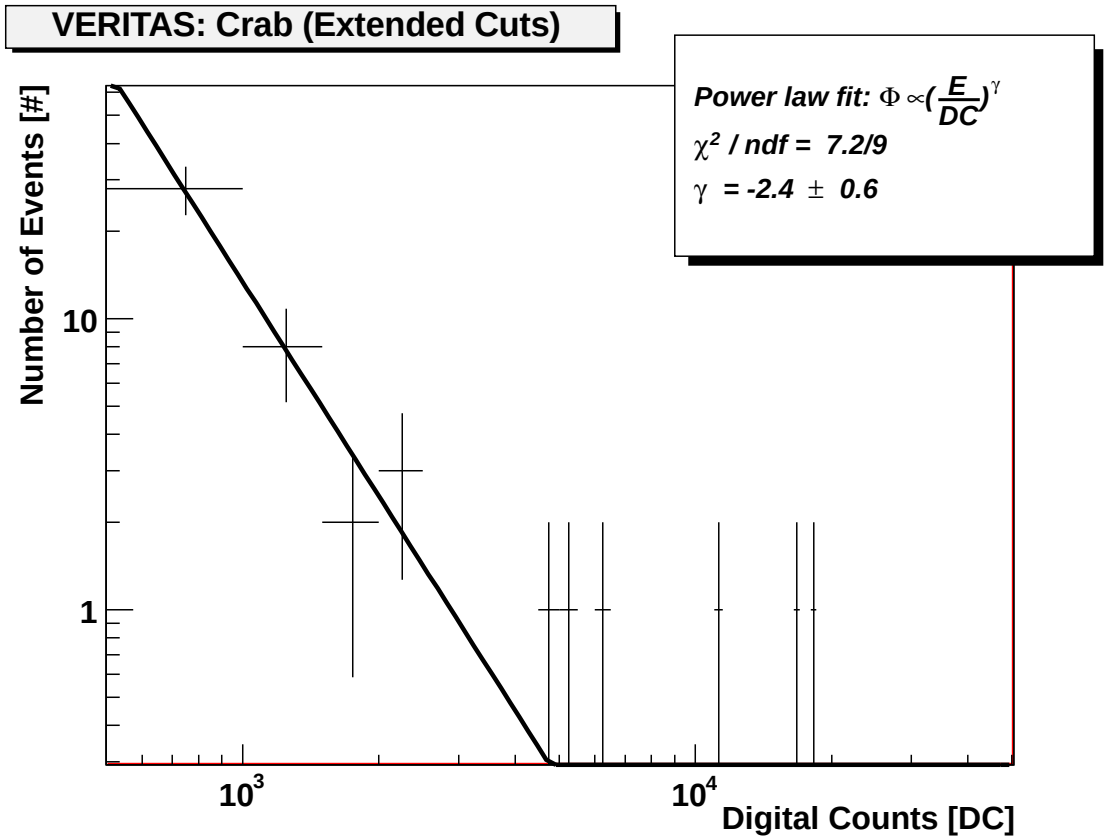

Figure 4.6. A histogram of the excess events (OFF events subtracted from the ON events) from the Crab nebula spectrum analysis.

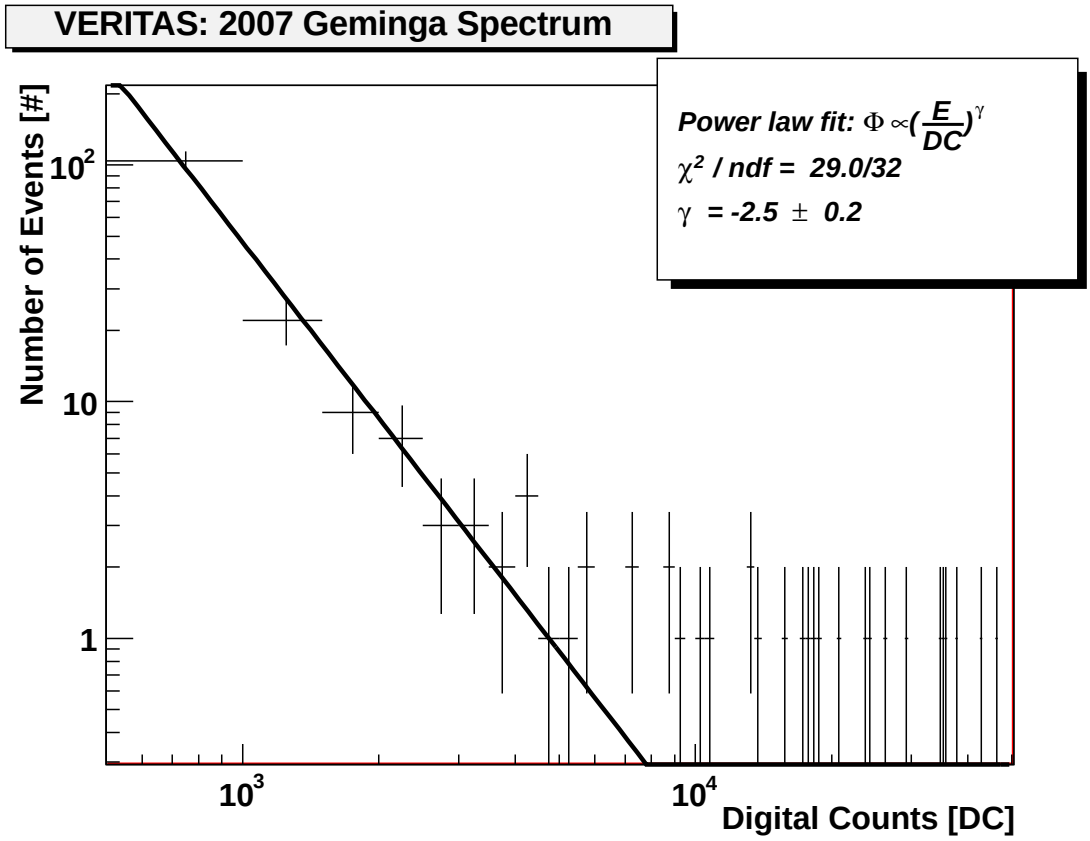

Figure 4.7. The total integrated digital counts for the 2007 data of each event of the ON runs minus the OFF runs.

5σ pretrials region was obtained (see Figure 4.9). A spectral analysis was also done on the 2010 data in the same manner as the 2007 data (see Figure 4.10). A spectral index of -2.6 ± 0.7 with a reduced $\chi^2 \sim 1$ was obtained.

4.2.5 2011 Data

Additional observations of Geminga were made in 2011/2012 observation season with the data selection criteria cuts described in Table 4.4. The observation mode was ON only (exactly like ON-OFF observations but with no OFF runs). OFF runs were matched to the ON runs in the same process as the 2007 data. In order to minimize the trials factor for the 2011 data, an a priori search region is defined by the circle of radius 0.75° centered at $RA, DEC = 99°,\ 17.8°$. A conservative estimate on the number of spacial trials in the search region is 100. The same cuts that where applied to the 2007 and 2010 data will be

Table 4.3. Data selection criteria cuts for the 2010 Geminga data. T_{on} and T_{off} are the duration of the total observations for the ON and OFF off runs, respectively.

Number of ON Hours (hours)	Integration Region (degrees sq.)	Minimum Number of PMTs	Minimum Digital Counts	Width Interval (degrees)	Impact Distance/ Length (m/degrees)
14.2	0.08	2	500	0.045-0.09	1.8-8.0

Average Zenith Angle (ON/OFF)	α (T_{on}/T_{off})
$16.4^{\circ}/16.5^{\circ}$	0.9517

applied. A 4.4σ excess was observed.

Figures 4.11 and 4.12 show the excess events (significance) from the 2011 data. The spectral analysis (Figure 4.13) was also completed. A hot spot with a significance greater than four sigma appears at $RA, DEC = X, Y$. The spectral analysis shows a spectral index of -2.1 ± 0.4. The posttrials significance for 100 trials is 3.2σ. Table 4.5 gives a summary of all three observing seasons.

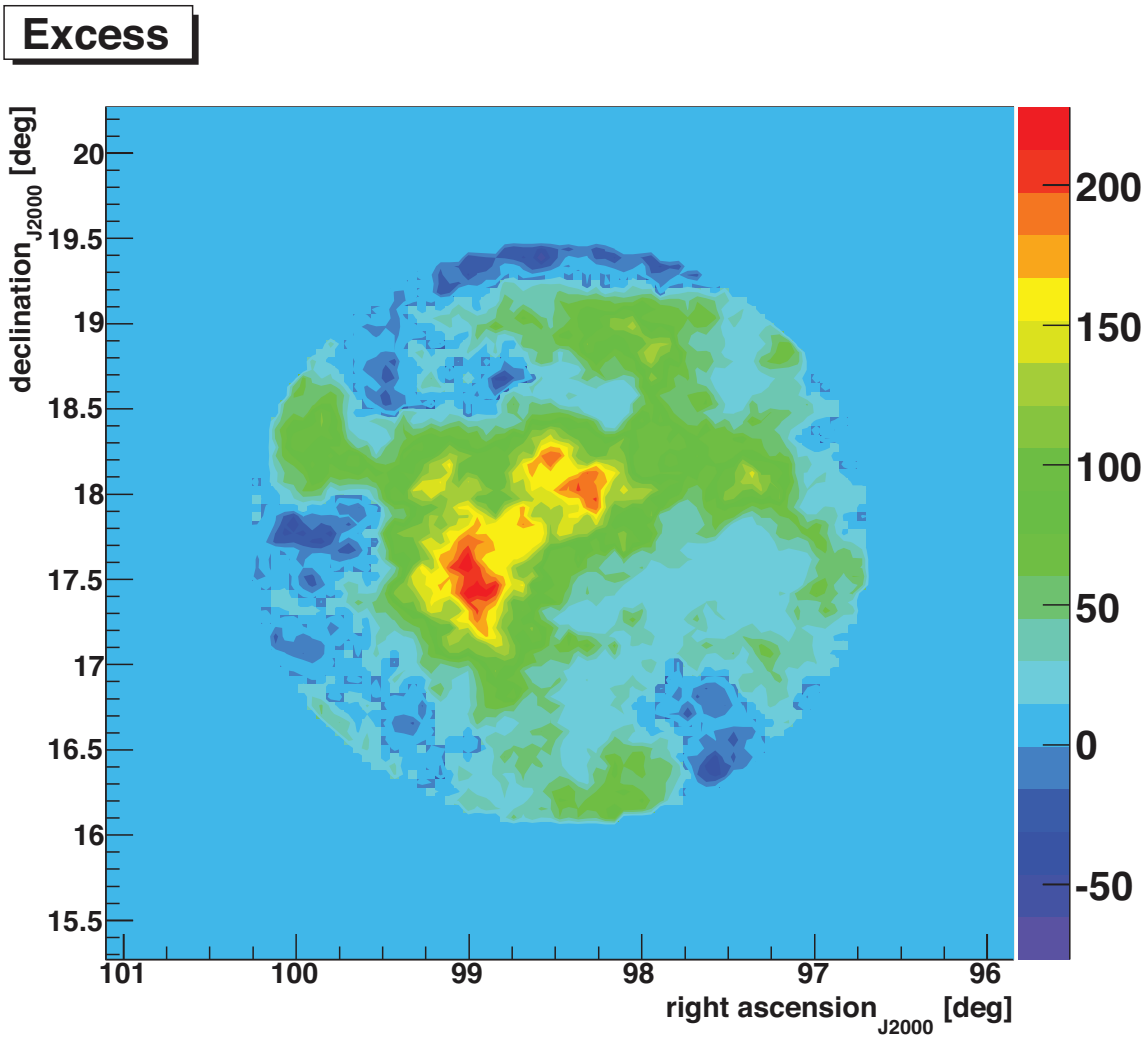

Figure 4.8. The excess map of the 2010 ON-OFF data.

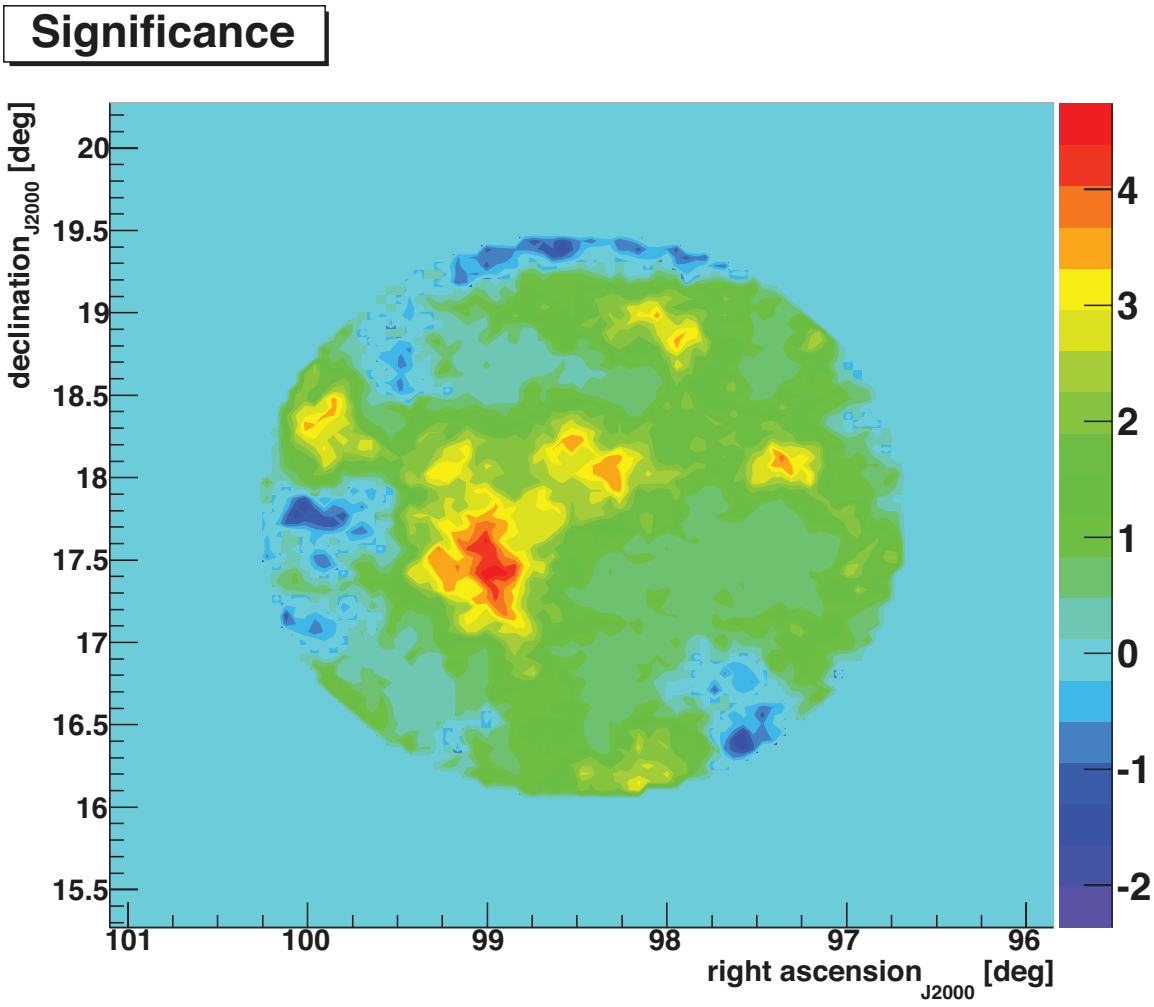

Figure 4.9. The significance map of the 2010 ON-OFF data.

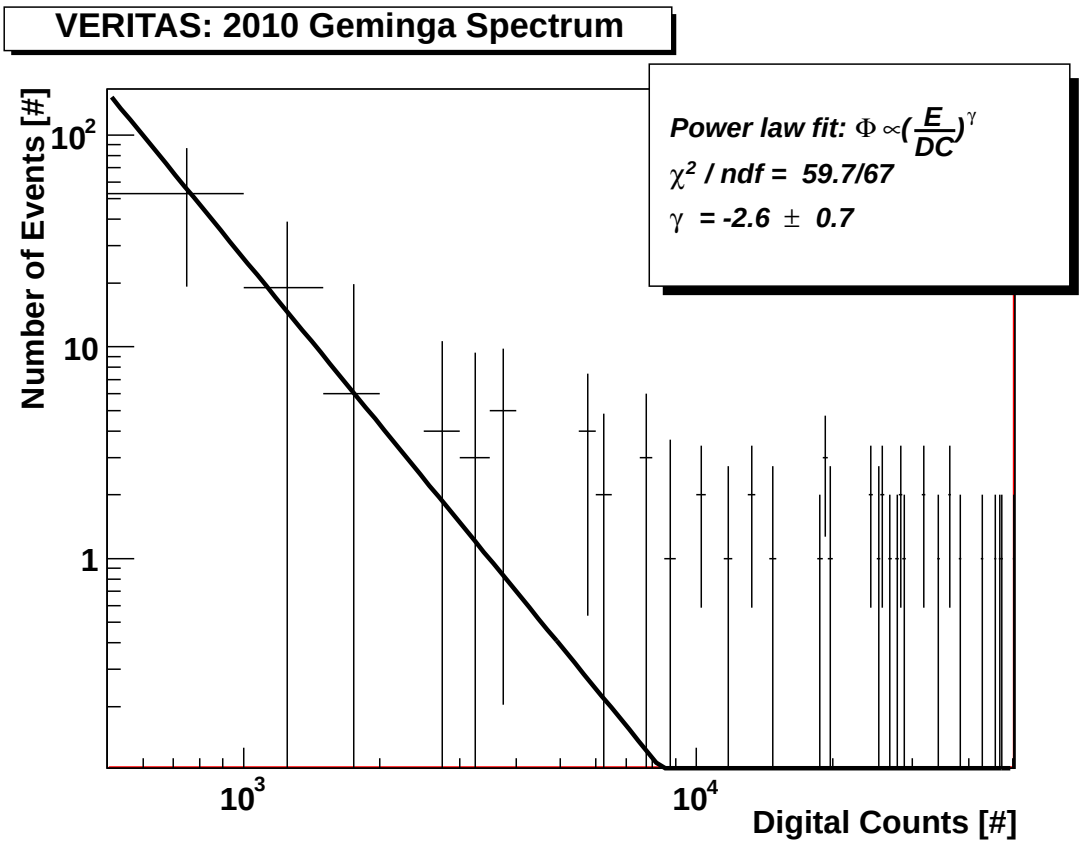

Figure 4.10. The total integrated digital counts for the 2010 data of each event of the ON runs minus the OFF runs.

Table 4.4. Data selection criteria cuts for the 2011 Geminga data. T_{on} and T_{off} are the duration of the total observations for the ON and OFF off runs, respectively.

Number of ON Hours (hours)	Integration Region (degrees sq.)	Minimum Number of PMTs	Minimum Digital Counts	Width Interval (degrees)	Impact Distance/ Length (m/degrees)
17.3	0.08	2	500	0.045-0.09	1.8-8.0

Average Zenith Angle (ON/OFF)	α (T_{on}/T_{off})
21.1°/24.5°	1.018

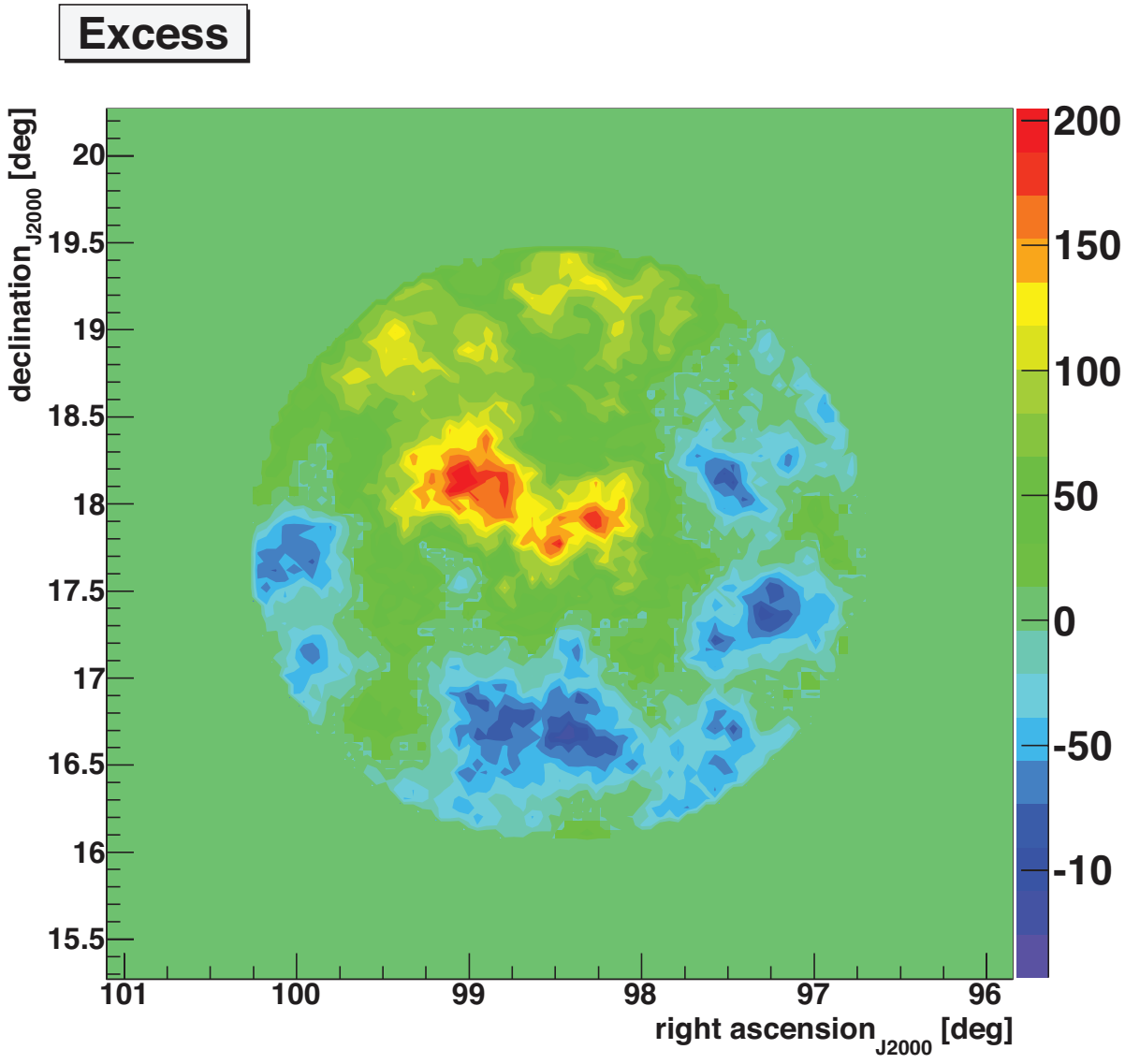

Figure 4.11. The excess map of the 2011 ON-OFF data.

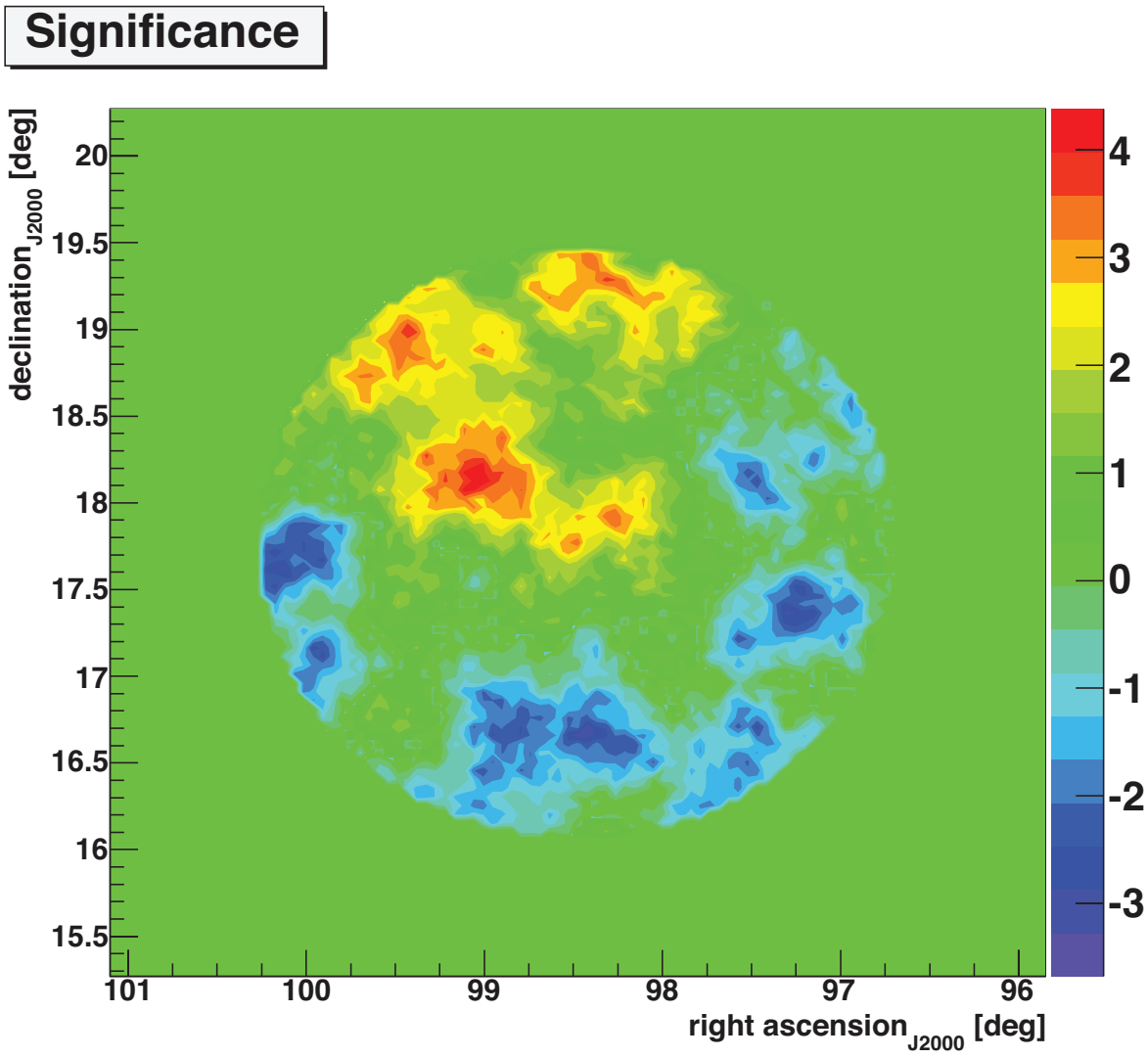

Figure 4.12. The significance map of the 2011 ON-OFF data

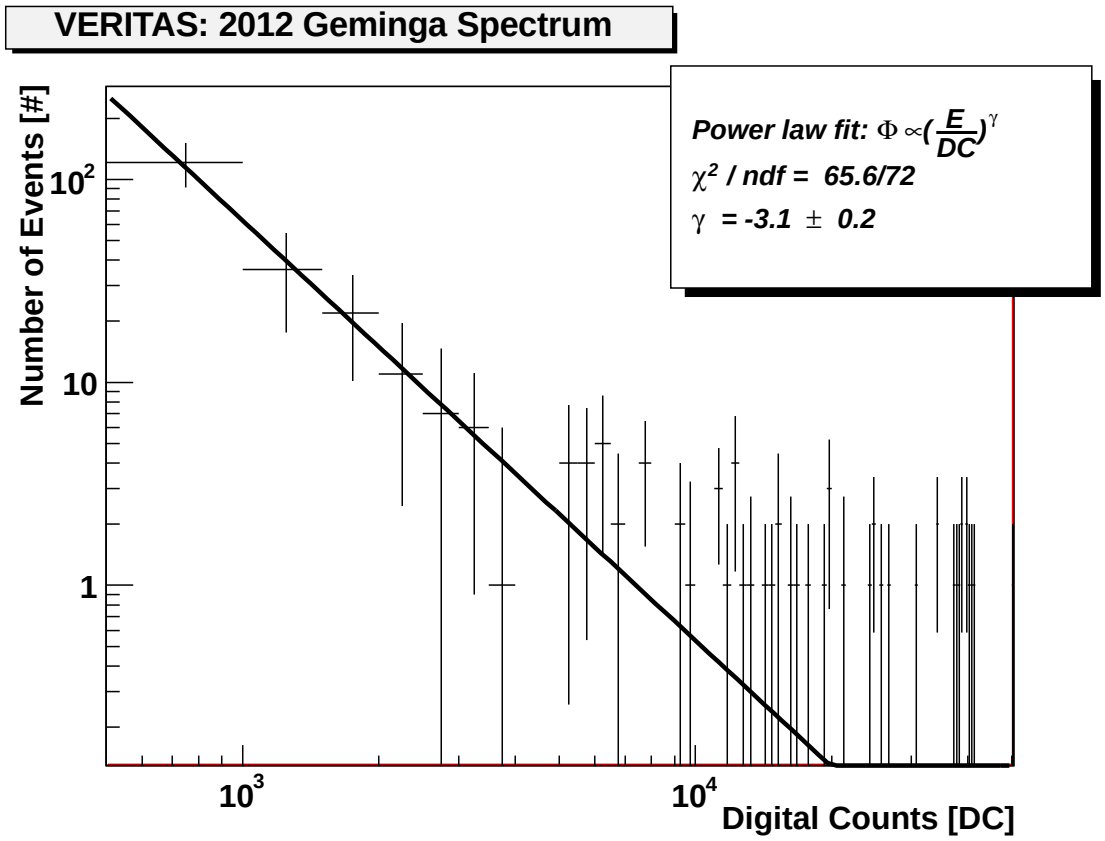

Figure 4.13. The total integrated digital counts for the 2011 data of each event of the ON runs minus the OFF runs.

Table 4.5. Summary table of the 2007, 2010, and 2011 data.

Year	Observation Mode	Pretrial Significance	Posttrial Significance	Spectral Index	Observation Hours	Average Zenith Angle (ON/OFF)
2007	Wobble	$> 5\sigma$	-	-2.5 ± 0.2	14.9	17.6°/21.1°
2010	ON-OFF	$\sim 5\sigma$	-	-2.6 ± 0.7	14.2	16.4°/16.5°
2011	ON	4.4σ	3.2σ	-3.1 ± 0.2	17.3	21.1°/24.5°
Average weighted spectral index: -2.8 ± 0.2						

CHAPTER 5

CONCLUSIONS

5.1 Summary

In order for VERITAS to detect a highly extended source such as Geminga, an analysis that would estimate the cosmic-ray background outside of the region near Geminga had to be developed. An ON-OFF analysis was chosen to analyze the 2007, 2010, and 2011 data. The standard analysis methods for VERITAS measure the significance of each bin in the excess map using the method described by Li & Ma (1983). Li and Ma made the observation that the resulting significance distribution appeared like a normal distribution and compared their results against it. Analysis of a point source object will produce a distribution of significances that appear to be of a normal distribution, with the mean centered at zero and with a width of one. It was shown in this dissertation that for an extended object, this may not hold true, and that the mean and the width of the distribution will increase. It was also shown that if the background was systematically underestimated, then the mean of the distribution also increases.

The data analysis done in this dissertation has been performed using a single analysis package, GrISU. The VERITAS Collaboration requires that all published source detections have at least two independent detections from different analysis packages; each detection should have a posttrails significance $> 5\sigma$, and there should be agreement on the implied flux and energy spectrum. The secondary independent analysis is currently in progress. We are not claiming an official VERITAS source detection in this dissertation, but are showing strong evidence for TeV emission from the Geminga region using the GrISU analysis package optimized for extended sources.

The VERITAS telescopes have observed Geminga during three observing seasons. Each data set from the individual seasons show strong evidence that an extended emission exists in the Geminga region. The pretrial significance for each of the observations is between 4 and 5σ. Due to the large extension and offset from the actual pointing position of the excess

as seen in the excess maps, the posttrials significance is decreased due to spacial trials (see Section 2.4). The 2012 posttrials significance is 3.2σ. Each data set was approximately 15 hours in total duration, resulting in a greater than 4σ significance level. To reach a level of 6σ (for a posttrials significance of 5σ with 100 trials), with the current VERITAS hardware and software configuration, the time needed to detect the source is approximately 36 hours.

A preliminary spectral analysis was performed on the Geminga data. The 2007, 2010, and 2011 data show evidence of a spectral index at the most significant bins of each data set of -2.5 ± 0.2, -2.6 ± 0.7, and -3.1 ± 0.4, respectively. When a more significant detection of Geminga is made, a complete spectral analysis could be performed. An extrapolation from the 2009 Milagro data point at 35 TeV to 1 TeV, using a spectral index of -2.6, gives an approximate differential flux of $4 \times 10^{-12} cm^{-2} s^{-1} TeV^{-1}$. This differential flux, over the entire extended area, is approximately 25% of the Crab Nebula (the standard candle for TeV astronomy). With the current VERITAS sensitivity, VERITAS should be able to detect a 25% Crab source (point-like in spacial resolution) in less than one hour. Since the full emission of Geminga is not compacted into a region smaller than the VERTIAS PSF but rather into a diffuse area, and the cosmic ray rate used to determine the background is constant for either a point source or an extended source, the differences in the signal and the background rate will be smaller than a 25% Crab nebula-like point source. Therefore, time needed to detect a 25% Crab extended source at a significant level is higher. The current analysis (assuming a Crab-like spectrum) suggests that the TeV emission from the Geminga SNR is approximately $1.5 \times 10^{-12} TeV\ cm^{-2}\ s^{-1}$ (Figure 5.1), which is at a level of a 4% of the Crab nebula.

5.2 Interpretation of Results

The HESS collaboration (Aharonian et al. 2006b) has detected the Vela X nebula in TeV gamma rays. The Vela X nebula has a spatially extended TeV emission of $0.48^\circ \pm 0.03^\circ$ by $0.36^\circ \pm 0.03^\circ$ (68% containment of the major and minor axis of a fitted ellipse). The distance to Vela X is $\sim$ 290pc (Dodson et al. 2003); therefore, the extended TeV emission from the HESS observations would have a physical extension of 5.1 parsecs along the major axis and 3.8 parsecs along the minor axis. The Milagro measurement of 2.8°, with a distance of approximately 200 parsecs, places the physical extension of this emission of Geminga to $\sim$ 10 parsecs. Many other SNRs have an extension on the order of a few parsecs. The excess maps of the VERITAS observations (see Figures 4.3, 4.8, and 4.11) reveal a possible

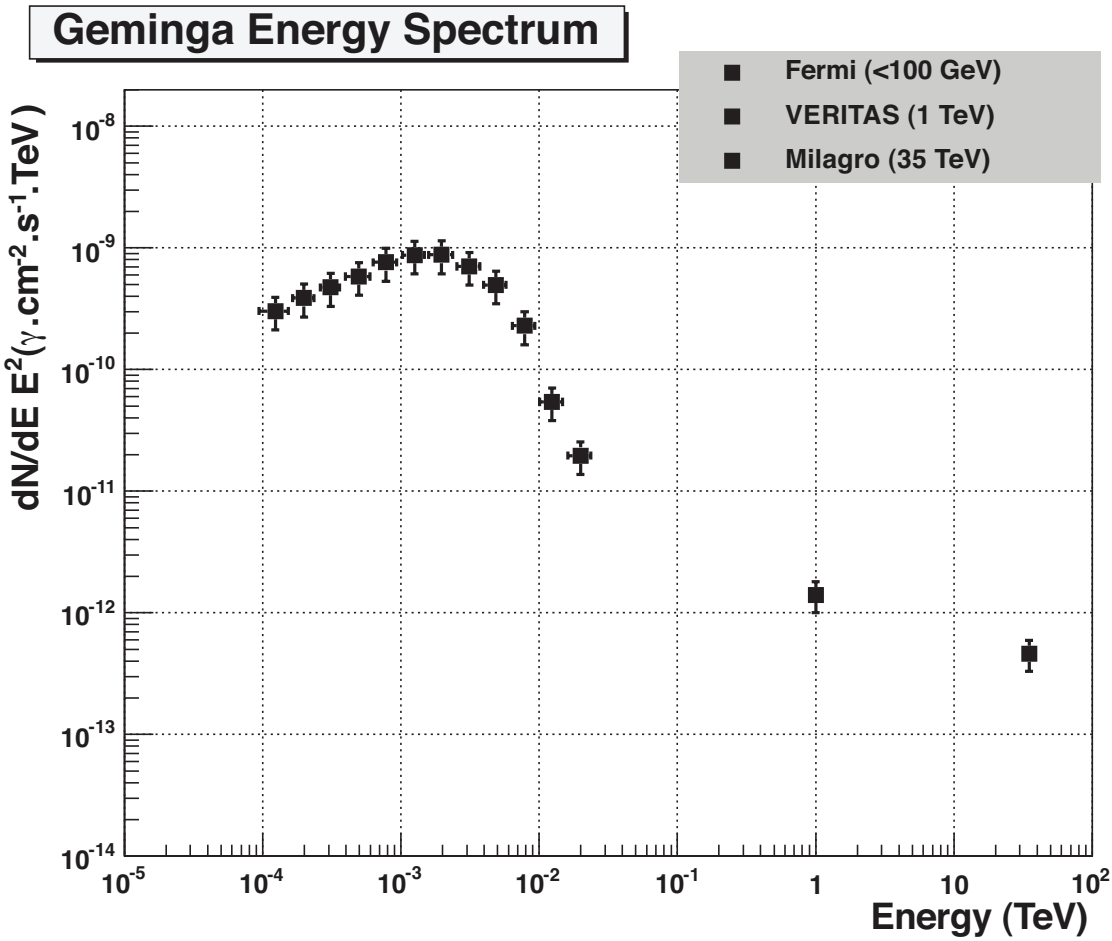

Figure 5.1. Spectral energy distribution of the Geminga pulsar ($< 0.1TeV$) and the Geminga diffuse source.

excess with an extension approximately one degree wide, placing the extension of Geminga to approximately 4 parsecs ($\sim$ 13 light years). The extension of Geminga is reasonable when comparing it to other SNRs. The proximity makes the Geminga SNR one of the most angularly extended astrophysical objects known.

A luminosity for energies greater than 1 TeV for Geminga can be determined by using the estimated flux. Luminosities for Vela and the Crab Nebula are also calculated (Table 5.1). $L/\dot{E}$ gives the fraction of energy from the pulsar spin-down luminosity that is converted to energies greater than 1 TeV. The data ($L/\dot{E}$) suggest that the older pulsars, Geminga and Vela, convert the pulsar spin-down energy more efficiently into TeV energies than a younger

Table 5.1. Comparison of luminosities ($E > 1\,TeV$) and age of Vela, Crab, and Geminga

Pulsar	Luminosity (L) ($E > 1TeV$)	$\dot{E}$ (Spin-down)	$L/\dot{E}$	Characteristic Age
Vela	$1.3 \times 10^{26} W$	$6.9 \times 10^{29} W$	0.00019	1.2×10^4 years
Geminga	$2.2 \times 10^{24} W$	$3.3 \times 10^{27} W$	0.00069	3×10^5 years
Crab	$5.8 \times 10^{27} W$	$4.6 \times 10^{31} W$	0.00013	1240 years

pulsar such as the Crab pulsar.

Advances in the VERITAS analysis are currently being developed. Improvements in the event reconstruction method are showing an improvement of 20% in sensitivity (Christiansen & the VERITAS Collaboration 2012). Better gamma ray and cosmic ray separation methods (Le Bohec et al. 1998) are being developed by the VERITAS collaboration by modeling the detected Cherenkov light of the EAS. A major hardware upgrade is being made to the VERITAS telescopes (Kieda & the VERITAS Collaboration 2011) that should allow a better detection of low-energy gamma-ray events. With the improvements in the analysis and hardware, and the current evidence of TeV emission from Geminga, VERITAS has the capabilities to make a firm detection of the Geminga extended source.

REFERENCES

Abdo, A. A., et al. 2007, Astrophys. J., 664, L91

—. 2009a, Science, 325, 840

—. 2009b, Astrophys. J., 696, 1084

—. 2009c, Astrophys. J., Suppl. Ser., 183, 46

—. 2009d, Astrophys. J., Lett., 700, L127

—. 2010a, Astrophys. J., 708, 1254

—. 2010b, Astrophys. J., 720, 272

Abdulwahab, M., & Morrison, P. 1978, Astrophys. J., 221, L33

Acciari, V. A., et al. 2008, Astrophys. J., 679, 1427

—. 2009, Astrophys. J., Lett., 698, L133

Acero, F., et al. 2009, Science, 326, 1080

Aharonian, F., et al. 1999, Astron. Astrophys., 346, 913

—. 2001, Astron. Astrophys., 370, 112

—. 2006a, Astron. Astrophys., 448, L43

—. 2006b, Astron. Astrophys., 448, L43

Aharonian, F. A., et al. 2007, Astron. Astrophys., 469, L1

Albert, J., et al. 2007, Astrophys. J., Lett., 664, L87

Alfvén, H., & Herlofson, N. 1950, Physical Review, 78, 616

Aliu, E., et al. 2008, Science, 322, 1221

Arons, J. 1981, in IAU Symposium, Vol. 95, Pulsars: 13 Years of Research on Neutron Stars, ed. W. Sieber & R. Wielebinski, 69–85

Berge, D., Funk, S., & Hinton, J. 2007, Astron. Astrophys., 466, 1219

Bertsch, D. L., et al. 1992, Nature, 357, 306

Bethe, H., & Heitler, W. 1934, Royal Society of London Proceedings Series A, 146, 83

Bignami, G. F., Caraveo, P. A., & Lamb, R. C. 1983, Astrophys. J., Lett., 272, L9

Bignami, G. F., Caraveo, P. A., & Mereghetti, S. 1993, Nature, 361, 704

Blackett, P. M. S. 1948, in The Emission Spectra of the Night Sky and Aurorae, 34

Blumenthal, G. R., & Gould, R. J. 1970, Reviews of Modern Physics, 42, 237

Bongiorno, S. D., Falcone, A. D., Stroh, M., Holder, J., Skilton, J. L., Hinton, J. A., Gehrels, N., & Grube, J. 2011, Astrophys. J., 737, L11

Caraveo, P. A., Bignami, G. F., De Luca, A., Pellizzoni, A., Mereghetti, S., Mignani, R. P., Tur, A., & Becker, W. 2004, Memorie della Societ Astronomica Italiana, 75, 470

Caraveo, P. A., Bignami, G. F., Mignani, R., & Taff, L. G. 1996, Astrophys. J., 461, L91

Caraveo, P. A., De Luca, A., Mignani, R. P., & Bignami, G. F. 2001, Astrophys. J., 561, 930

Cavallo, G., & Gould, R. J. 1971, Nuovo Cimento B Serie, 2, 77

Celik, O., & the VERITAS Collaboration. 2011, arXiv:0709.3686

Chang, J., et al. 2008, Nature, 456, 362

Cheng, K. S., Ho, C., & Ruderman, M. 1986, Astrophys. J., 300, 500

Christiansen, J., & the VERITAS Collaboration. 2012, Proceedings of the 5th International Symposium on High-Energy Gamma-Ray Astronomy

Claussen, M. J., Frail, D. A., Goss, W. M., & Gaume, R. A. 1997, Astrophys. J., 489, 143

Davies, J. M., & Cotton, E. S. 1957, J. Solar Energy Sci. and Eng., 1, 16

de Naurois, M. 2007, Astrophys. Space. Sci., 309, 277

de Naurois, M., et al. 2002, Astrophys. J., 566, 343

Dodson, R., Legge, D., Reynolds, J. E., & McCulloch, P. M. 2003, Astrophys. J., 596, 1137

Ellis, J., Fields, B. D., & Schramm, D. N. 1996, Astrophys. J., 470, 1227

Faherty, J., Walter, F. M., & Anderson, J. 2007, Astrophys. Space. Sci., 308, 225

Fichtel, C. E., Hartman, R. C., Kniffen, D. A., Thompson, D. J., Ogelman, H., Ozel, M. E., Tumer, T., & Bignami, G. F. 1975, Astrophys. J., 198, 163

Finnegan, G., & the VERITAS Collaboration. 2011, arXiv:1111.0121

Gaensler, B. M., & Slane, P. O. 2006, Ann. Rev. Astron. Astrophys., 44, 17

Galbraith, W., & Jelley, J. V. 1953, Nature, 171, 349

Garcia-Munoz, M., Mason, G. M., & Simpson, J. A. 1977, Astrophys. J., 217, 859

Gold, T. 1968, Nature, 218, 731

Goldreich, P., & Julian, W. H. 1969, Astrophys. J., 157, 869

Halpern, J. P., & Holt, S. S. 1992, Nature, 357, 222

Heitler, W. 1954, Quantum Theory of Radiation (3rd ed.; Oxford: Clarendon)

Helene, O. 1983, Nuclear Instruments and Methods in Physics Research, 212, 319

Hermsen, W., et al. 1977, Nature, 269, 494

Hillas, A. M. 1996, Space Sci. Rev., 75, 17

Holder, J., et al. 2006, Astroparticle Physics, 25, 391

Huang, Y.-L., & Thaddeus, P. 1986, Astrophys. J., 309, 804

Jackson, M. S., & Halpern, J. P. 2005, Astrophys. J., 633, 1114

Kaplan, D. L., Chatterjee, S., Gaensler, B. M., & Anderson, J. 2008, Astrophys. J., 677, 1201

Kassim, N. E., & Lazio, T. J. W. 1999, Astrophys. J., 527, L101

Kieda, D. 2008, in American Institute of Physics Conference Series, Vol. 1085, American Institute of Physics Conference Series, ed. F. A. Aharonian, W. Hofmann, & F. Rieger, 269–272

Kieda, D., & the VERITAS Collaboration. 2011, in International Cosmic Ray Conference, Vol. 9, International Cosmic Ray Conference, 14

Le Bohec, S. 2009, http://www.physics.utah.edu/gammaray/GrISU/

Le Bohec, S., et al. 1998, Nuclear Instruments and Methods in Physics Research A, 416, 425

Lessard, R. W., et al. 2000, Astrophys. J., 531, 942

Li, T.-P., & Ma, Y.-Q. 1983, Astrophys. J., 272, 317

Longair, M. S. 2011, High Energy Astrophysics

Lorimer, D. R., & Kramer, M. 2005, Handbook of Pulsar Astronomy

Maier, G. 2011, in International Cosmic Ray Conference, Vol. 7, International Cosmic Ray Conference, 82

McLean, B. J., Greene, G. R., Lattanzi, M. G., & Pirenne, B. 2000, in Astronomical Society of the Pacific Conference Series, Vol. 216, Astronomical Data Analysis Software and Systems IX, ed. N. Manset, C. Veillet, & D. Crabtree, 145

Mostafa, M. 2011, in International Cosmic Ray Conference, Vol. 9, International Cosmic Ray Conference, 69

Olbert, C. M., Clearfield, C. R., Williams, N. E., Keohane, J. W., & Frail, D. A. 2001, Astrophys. J., Lett., 554, L205

Pavlov, G. G., Bhattacharyya, S., & Zavlin, V. E. 2010, Astrophys. J., 715, 66

Pavlov, G. G., Sanwal, D., & Zavlin, V. E. 2006, Astrophys. J., 643, 1146

Perkins, J. S., Maier, G., & The VERITAS Collaboration. 2009, ArXiv:0912.3841

Salvati, M., & Sacco, B. 2008, Astron. Astrophys., 485, 527

Schödel, R., et al. 2002, Nature, 419, 694

Sturrock, P. A. 1971, Astrophys. J., 164, 529

Tepe, A., & the HAWC Collaboration. 2012, Journal of Physics Conference Series, 375, 052026

Thompson, D. J., Fichtel, C. E., Hartman, R. C., Kniffen, D. A., & Lamb, R. C. 1977, Astrophys. J., 213, 252

VERITAS Collaboration et al. 2009, Nature, 462, 770

—. 2011, Science, 334, 69

Völk, H. J., Aharonian, F. A., & Breitschwerdt, D. 1996, ssr, 75, 279

Weekes, T. C. 2003, Very high energy gamma-ray astronomy

Yüksel, H., Kistler, M. D., & Stanev, T. 2009, Physical Review Letters, 103, 051101

Yun, M. S., Ho, P. T. P., & Lo, K. Y. 1994, Nature, 372, 530